Aalto University
School of Electrical Engineering
Degree Programme in Electronics and Electrical Engineering

Juha-Matti Tilli

Composition determination of quaternary GaAsPN

Master's Thesis
Espoo, August 1, 2014

Supervisor: Professor Harri Lipsanen
Advisor: Henri Jussila M.Sc. (Tech.)

Aalto University
School of Electrical Engineering
Degree Programme in Electronics and Electrical Engineering

ABSTRACT OF MASTER'S THESIS

Author:	Juha-Matti Tilli		
Title:	Composition determination of quaternary GaAsPN		
Date:	August 1, 2014	**Pages:**	10 + 96
Major:	Micro and Nanosciences	**Code:**	S-104
Supervisor:	Professor Harri Lipsanen		
Advisor:	Henri Jussila M.Sc. (Tech.)		

30 nm and 130 nm thick Ga(As)PN epilayers were grown on a GaP substrate to study whether it is possible to determine their composition using various measurement techniques not typically used for quaternary material composition definition. Specifically, the techniques that were most promising were using a single X-ray diffraction (XRD) scan of a quasi-forbidden (002) reflection and using X-ray reflectivity (XRR) electron density in addition to XRD peak location. The intensity of this (002) reflection varies as a function of arsenic content, which allows having two free composition-related variables, peak intensity and location. The obtained layer compositions are compared with accurate reference values obtained with Rutherford backscattering spectroscopy combined with nuclear reaction analysis measurements. The results reveal that the XRD method overestimates the arsenic and nitrogen content with an error margin of about 0.12 in arsenic content and 0.025 in nitrogen content for the 30 nm thick films, but the accuracy can be improved by taking peak weakness into account. The XRR and XRD based method is more accurate with accuracy being 0.05 in arsenic content and 0.01 in nitrogen content. Furthermore, a method is demonstrated to determine the layer composition with photoreflectance inverting the two-level band anticrossing model to determine material composition based on the energies of the transitions from the valence band to the split conduction band.

Keywords:	GaAsPN, quaternary semiconductor, X-ray diffraction, Rutherford backscattering, photoreflectance
Language:	English

Aalto-yliopisto
Sähkötekniikan korkeakoulu
Elektroniikan ja sähkötekniikan koulutusohjelma

DIPLOMITYÖN
TIIVISTELMÄ

Tekijä:	Juha-Matti Tilli		
Työn nimi:	Neliyhdistepuolijohde GaAsPN:n koostumuksen määritys		
Päiväys:	1. elokuuta 2014	**Sivumäärä:**	10 + 96
Pääaine:	Mikro- ja nanotekniikka	**Koodi:**	S-104
Valvoja:	Professori Harri Lipsanen		
Ohjaaja:	Diplomi-insinööri Henri Jussila		

30 nm ja 130 nm paksuja Ga(As)PN-epikerroksia kasvatettiin GaP-substraatille, joiden avulla tutkittiin onko mahdollista määrittää kerrosten koostumus mittaustekniikoilla joita ei tavanomaisesti käytetä neliyhdistepuolijohteen koostumusmääritykseen. Erityisesti tekniikat jotka vaikuttivat lupaavimmilta olivat yhden kvasikielletystä (002)-heijastuksesta mitatun röntgendiffraktiokäyrän käyttäminen ja röntgenheijastuksella määritetyn elektronitiheyden käyttäminen röntgendiffraktiopiikin sijainnin lisäksi. Tämän heijastuksen intensiteetti muuttuu arseenipitoisuuden funktiona, mikä sallii kahden koostumusriippuvaisen vapaan muuttujan määrittämisen. Saatuja kerrosten koostumuksia vertaillaan tarkkoihin referenssiarvoihin, jotka on saatu Rutherford-takaisinsirontaspektroskopialla yhdistettynä ydinreaktioanalyysimittauksiin. Tulokset paljastavat, että röntgendiffraktiomenetelmä yliarvioi arseeni- ja typpipitoisuuksia arseenipitoisuuden virheen ollen noin 0.12 ja typpipitoisuuden virheen 0.025 30 nm paksuille kerroksille, mutta tarkkuutta voidaan parantaa. Röntgenheijastukseen ja röntgendiffraktioon pohjautuva menetelmä on tarkempi arseenipitoisuuden virheen ollen noin 0.05 ja typpipitoisuuden virheen 0.025. Lisäksi esitettiin menetelmä, jolla voidaan määrittää kerroksen koostumus fotoreflektanssilla invertoiden kaksitasoisen band anticrossing -mallin. Menetelmä antaa koostumuksen, kun tiedetään transitioiden energiat valenssivyöltä jakautuneelle johtavuusvyölle.

Asiasanat:	GaAsPN, neliyhdistepuolijohde, röntgendiffraktio, Rutherford-takaisinsironta, fotoreflektanssi
Kieli:	Englanti

Preface

This thesis has been carried out in the optoelectronics and nanotechnology groups of Aalto University. Parts of the work have also been published in Journal of Applied Physics in 2014 [1] and described in other articles not yet sent to any journal. The main studies have been performed during the summer 2013, but the work is a logical continuation of the work I did at Aalto University during the summers 2006-7 while developing X-ray diffraction and reflectivity software. I would like to thank professor Harri Lipsanen, professor Markku Sopanen and Veli-Matti Airaksinen for the opportunity to work there during the summers 2014, 2007 and 2013, and 2006.

I would like to thank the thesis advisor Henri Jussila for good instructions and many valuable comments on my work and for teaching me how to use the X-ray diffraction machine. Knowing in detail how the fitting analysis is performed and writing software to do that does not mean one is able to use the apparatus.

I would also like to thank Jouni Tiilikainen for introducing me to the world of X-ray reflectivity, without which I would not have developed the X-ray reflectivity and diffraction software during the summers 2006 and 2007. Also big thanks to Aapo Lankinen for instructing my BSc thesis [2] about X-ray diffraction.

Finally, I would like to thank my parents and my sister for encouraging me to continue my studies even though I considered abandoning my studies and continuing my work career.

Espoo, August 1, 2014

Juha-Matti Tilli

Author's contribution

The author has written the manuscript for this thesis, for the scientific article published in Journal of Applied Physics in 2014 [1] about this thesis and several other scientific articles to be submitted to a journal. The scientific articles have been subsequently proofread and modified by the co-authors. The author designed the sample growth parameters and the X-ray diffraction experiments for the 30 nm thick samples. The samples in this work have been grown either by the author, some with Jori Lemettinen and/or under the guidance of the advisor, or by the advisor, depending on the sample. The X-ray diffraction measurements have been performed either by the author, some under the guidance of the advisor, or by the advisor, depending on the sample. All of the X-ray reflectivity and X-ray diffraction simulations and the analysis of the X-ray diffraction measurements have been completely done by the author with custom software written by the author. The photoreflectance measurements have been performed by the author and Jori Lemettinen. The fitting of photoreflectance spectra was performed by the advisor. The analysis of material composition based on the photoreflectance transitions was performed by the author with custom software written by the author. The atomic force micrographs have been acquired either by the author under the guidance of the advisor, or by the advisor, depending on the sample. The Rutherford backscattering measurements have been performed and the results analyzed by Kin Man Yu from Lawrence Berkeley National Laboratory.

List of acronyms

AES	Auger electron spectroscopy
AFM	atomic force microscopy
ALD	atomic layer deposition
BAC	band anticrossing (model)
BJT	bipolar junction transistor
CMOS	complementary metal-oxide-semiconductor (field effect transistors)
DMHy	dimethylhydrazine
GaAs	gallium arsenide
GaAsP	gallium arsenide phosphide
GaAsPN	gallium arsenide phosphide nitride
GaP	gallium phosphide
GaPN	gallium phosphide nitride
HBT	heterojunction bipolar transistor
HEMT	high electron mobility transistor
HRXRD	high resolution X-ray diffraction
IBSC	intermediate-band solar cell
InAlAsSb	indium aluminium arsenide antimonide
LPE	liquid phase epitaxy
MBE	molecular beam epitaxy
MOSFET	metal-oxide-semiconductor field effect transistor
MOVPE	metalorganic vapor phase epitaxy
MQW	multiple quantum well

NRA	nuclear reaction analysis
PIPS	passivated implanted planar silicon (detector)
PL	photoluminescence
PR	photoreflectance
RBS	Rutherford backscattering spectroscopy
RSM	reciprocal space map
SIMS	secondary ion mass spectroscopy
SR-XRT	synchrotron radiation X-ray topography
TBAs	tertiarybutylarsine
TBP	tertiarybutylphosphine
TEM	transmission electron microscopy
TER	total external reflection
TMGa	trimethylgallium
UC-PV	up-converting photovoltaic (cell)
XPS	X-ray photoelectron spectroscopy
XRD	X-ray diffraction
XRF	X-ray fluorescence
XRR	X-ray reflectivity

Contents

1 Introduction

The semiconductor industry today is based mostly on CMOS circuits manufactured on silicon substrates. The advantages of silicon are low material cost, the availability of a high quality gate oxide and a reasonably high hole mobility in comparison to *e.g.* GaAs. Additionally, the temperature at which doped silicon becomes intrinsic is high, meaning that silicon transistors can operate at high temperatures when compared to *e.g.* germanium transistors. In MOSFETs built using the CMOS process, ideally current only flows when a transistor switches its state, leading to low power consumption in large integrated circuits, which explains why most integrated circuits today are made using the CMOS process. However, it should be mentioned that in modern sub-micrometer CMOS processes there is also a continuously flowing leakage current. There is also capacitive coupling between the electrical wires, which explains why optoelectronic interconnects are interesting. Silicon is also the dominant material in solar cells, which can be explained by the low cost of silicon substrates. However, silicon is a poor light emitter due to its indirect bandgap which explains why optoelectronic components are made from III-V compound semiconductors. Additionally, III-V compound semiconductors can be used to manufacture high-electron mobility transistors (HEMT) and heterojunction bipolar transistors (HBT) which have a higher cut-off frequency than conventional transistors. III-V dilute nitrides also have an effect where the conduction band splits into two [3–9], thus making it possible to fabricate an intermediate band solar cell (IBSC) [10–17].

The integration of III-V compound semiconductors with silicon could enable integrating high-frequency components and optoelectronics for inter-chip and intra-chip

interconnects with silicon CMOS technology. Additionally, a silicon intermediate band solar cell could compete with traditional silicon solar cells in terrestrial applications. Of all binary III-V compound semiconductors, gallium phosphide (GaP) has the smallest lattice mismatch when compared to silicon. Therefore, gallium phosphide is a promising buffer layer material for growing III-V compound semiconductors on top of silicon. In order to successfully fabricate components on top of silicon, viable components have to be demonstrated on gallium phosphide substrates first.

The quaternary material GaAsPN allows more degrees of freedom for adjusting the band gap and the lattice constant when compared to *e.g.* GaPN. A GaAsPN quantum well laser integrated on silicon has already been successfully demonstrated using electrical injection [18, 19]. The material also has drawn some attention in the solar cell research community due to having a split conduction band [20] allowing the fabrication of an IBSC. Furthermore, the material has been proposed to be used in fabrication of a silicon tandem solar cell [21]. However, the composition determination of this quaternary material is challenging. The traditional method to determine the composition of an epilayer is the determination of the lattice constant from XRD [22,23] measurements. However, with quaternary materials, determining the lattice constant from XRD measurements is not enough, as the composition determination of a quaternary material requires determining two variables. For the GaAsPN quantum well laser, it was noted that XRD allows precise composition determination of only ternary alloys, and the composition of the quaternary GaAsPN was determined by various test structures that investigated the incorporation behaviour of various elements in MOVPE [19]. There are several composition determination methods that work for quaternary materials such as AES [24, 25], SIMS [26], RBS [27, 28], XPS [29] and XRF [30]. However, the measurement apparatuses required for these methods are uncommon. *E.g.* an RBS system is rare, whereas an X-ray diffractometer is found in almost any optoelectronics laboratory. Similarly a PR measurement apparatus can be built from standard laboratory equipment.

In this thesis, new methods for composition determination based on XRD peak intensity, XRR electron density and band-anticrossing (BAC) model calculations

with PR measurements are developed. All of these methods allow the composition determination of the quaternary GaAsPN. Furthermore, a new manual method for performing a relaxation test with a triple-crystal diffractometer is developed to check that the layers are fully strained, which the XRD based composition determination assumes. This work could be expanded by developing a more comprehensive theory of dynamical XRD that takes into account the presence of crystallographic defects, but that is out of the scope of this work and would require specialized knowledge that the author does not have. The objective of this work is to determine whether the proposed XRR, XRD and PR based methods are accurate for the grown GaAsPN layers. The objective of this work is not to fully characterize the set of samples grown, but as a side effect of the studies done evidence about low crystalline quality and a composition gradient of N were found.

In Chapter 2, the theoretical basis related to III-V semiconductors and the growth of gallium phosphide on silicon is reviewed. In Chapter 3, the metal-organic vapor phase epitaxy (MOVPE) growth process is described. In Chapter 4, the used measurement methods XRR, XRD, PR, AFM and RBS/NRA are reviewed. In Chapter 5 the novel measurement methods based on XRD and PR are described. In Chapter 6 the results of the measurements are presented and discussed. Chapter 7 concludes this thesis.

2 Theoretical basis of the materials

This chapter reviews the theoretical basis of the materials used in this work. For the theoretical basis of the used growth and measurement methods, see the next chapters. First, III-V compound semiconductors and their growth methods in general are described. Then gallium phosphide based alloys are discussed.

2.1 III-V compound semiconductors

Silicon, the most common semiconductor material today, has an indirect band gap. To create luminescent components, a direct band gap is required. Many III-V compound semiconductors have a direct band gap. The crystal structure of III-V compound semiconductors is usually zinc blende or wurtzite. The III-nitrides naturally have a wurtzite structure and the other semiconductors generally have a zinc blende structure, but the incorporation of a small amount of nitrogen in III-V zinc blende compound semiconductors does not change the crystal structure.

For binary compound semiconductors, the lattice constant of the material is a known parameter. For ternary and quaternary semiconductors, the lattice constant can be calculated from Vegard's law [31, 32] which is a linear interpolation law for the lattice constant. In this thesis, a similar linear interpolation law has also been used for the parameters E_N and C_{MN} of the BAC model and the Poisson's ratio.

The band gap cannot be calculated from a simple linear interpolation law unlike

Table 2.1: Lattice constants and band gaps of silicon, germanium and III-V compound semiconductors having the zinc blende crystal structure. From the table we can see that the lattice constant of GaP is very close to that of silicon.

	a	E_g
Si	5.431 Å	1.12 eV
Ge	5.658 Å	0.661 eV
GaAs	5.65325 Å	1.424 eV
GaP	5.4505 Å	2.26 eV
InAs	6.0583 Å	0.354 eV
InP	5.8687 Å	1.344 eV

the other constants. There is a second-order bowing term in the law. For example, for $GaAs_yP_{1-y}$ the direct band gap is

$$E_{M\Gamma}(0) = (2.776 - 1.469y + 0.108y^2)\ \text{eV}. \tag{2.1}$$

GaP actually has an indirect band gap lower than the direct band gap. The previous equation calculates the direct band gap.

III-V compound semiconductor substrates are grown using *e.g.* the Czochralski process or the Bridgman method. Layers of III-V compound semiconductors on top of the substrate are grown with epitaxy. Epitaxy refers to the growth of crystalline thin films on top of a crystal substrate. The growth can be either homoepitaxial where the same material as the substrate crystal is grown on top of it, or heteroepitaxial where a different material is grown. At a glance, homoepitaxy may sound pointless, but the grown film can be more pure than the substrate and can have a different level of doping than the substrate. In the case of heteroepitaxy, the lattice constant mismatch between the substrate and the grown film results in strain parallel to the surface. An opposite strain in the direction perpendicular to the surface results from strain parallel to the surface, and can be calculated from the Poisson's ratio. Both homoepitaxy and heteroepitaxy were used in this thesis: the growth of a

gallium phosphide (GaP) buffer layer on top of the GaP substrate is homoepitaxial growth, while the growth of GaAsPN on top of GaP is heteroepitaxial growth.

In addition to luminescent components, III-V compound semiconductors enable a lot of interesting applications such as transistors having a higher cut-off frequency than silicon MOSFETs and BJTs. Additionally, multi-junction solar cells can be manufactured with III-V compound semiconductors. To understand why multi-junction solar cells are important, it can be noted that basic crystalline silicon solar cells have a Shockley-Queisser limit of 30 percent [33] and have reached an efficiency of 25 percent in non-concentrated light. A fundamental limitation here is that at energies lower than the band gap, the material of the solar cell does not absorb light, and with photon energies higher than the band gap, the excess energy is lost as heat. Multi-junction solar cells have multiple junctions with band gap energies decreasing in the deeper junctions, allowing light absorption at different wavelengths. GaAs multijunction solar cells have reached an efficiency of 44 percent in concentrated light and 38 percent in non-concentrated light.

Conventional solar cells have only two relevant energy bands: the valence band and the conduction band and there is only one possible transition from the valence band to the conduction band. Adding a new energy band to an n-band solar cell adds n new transitions: for example for a two-band one-transition solar cell, adding an intermediate band results in a total of three transitions. Such a solar cell could compete with a three-junction solar cell while having a far simpler structure and therefore potentially lower cost. In III-V dilute nitrides, the BAC model predicts that the conduction band splits into two sub-bands. Thus these materials can be used to fabricate a multi-band solar cell.

In terrestrial applications the figure of merit is watts per cost which results in cheap silicon-based cells dominating the market. In space applications, where the launch cost is high, the figure of merit is watts per kilogram. High-efficiency multijunction solar cells are used in satellites and space exploration, and in terrestrial applications when combined with solar concentrators. It has been predicted that in the future, electric power generation is dominated by solar cells. However, solar cells are unable to produce power when the sun doesn't shine, and electricity is

hard to store. Therefore, it is likely that in the future concentrated solar-thermal power plants that store heat in the daytime and use it to generate electricity during the nighttime are needed in addition to photovoltaic cells to achieve an ecological electricity generation mix. Fortunately, electricity use peaks in the daytime when the sun shines, so there is also need for solar cells in the power generation mix, too. Currently solar cells are used mainly in terrestrial off-grid applications and in space where an electric grid is not available.

Fabricating an intermediate-band solar cell from III-V dilute nitrides could make it possible to use low cost silicon wafers as the substrate of the solar cell. In this application, an intentionally miscut substrate can be used to reduce the amount of monoatomic steps [34] and thus the degree of anti-phase disorder, because no CMOS electronics are going to be integrated with the solar cell. It should be noted that there is also another way to increase the efficiency of silicon solar cells, namely the upconverting photovoltaic (UC-PV) cell [35]. Such solar cells have a backside layer made of an upconverting material which absorbs multiple photons at low energies and re-emits a single photon at a high energy.

2.2 Gallium phosphide based alloys

Of the binary III-V semiconductors, gallium phosphide (GaP) has a lattice constant closest to that of silicon. For this reason, gallium phosphide looks to be a promising buffer layer for the integration of III-V based components such as high-speed transistors and optoelectronics on silicon substrates. GaP growth on silicon has been investigated as early as 1980 [36,37]. However, it has only been recently shown that a suitable buffer layer of gallium phosphide can be grown on silicon [38–48]. After that, it was shown that GaAsPN MQW structures having direct band gap can be grown on GaP [49–51] and monolithically integrated on silicon [52]. Furthermore, it was shown that GaAsPN MQW structures achieve lasing under optical injection [53] and can be used in the fabrication of a laser diode on GaP [54–57]. Then a laser integrated on silicon was successfully demonstrated using electrical injection [18,19].

In this work, the composition determination of GaAsPN is done on gallium phosphide substrates and thus GaP is not grown on silicon, but gallium phosphide is an interesting material precisely because it can be grown on silicon.

Gallium phosphide has an indirect band gap. However, gallium phosphide and gallium arsenide phosphide based dilute nitride materials where a few percent of nitrogen is included in the alloy change the indirect bandgap to a direct one, making it possible to fabricate light-emitting components. Additionally, nitrogen changes the band structure in a significant and important way: the conduction band of dilute nitrides has been observed to split into two sub-bands. In an intermediate-band solar cell, the intermediate band needs to be isolated from the contacts and the open circuit voltage is determined by the E_+ band. In lasers and light-emitting diodes, the intermediate band is not isolated from the contacts and thus the intermediate E_- band determines the wavelength of the emitted light. This enables the emission at a wavelength longer than the direct band gap of GaP.

Gallium phosphide is a binary semiconductor, and therefore growing it on a monoatomic semiconductor can lead to so-called anti-phase disorder. For this reason among others, the growth of GaAsPN is done on gallium phosphide substrates in this work to prevent anti-phase disorder from affecting the XRD results. As a matter of fact, the (002) reflection has been used to determine the degree of anti-phase disorder previously [58]. This illustrates the importance of the used GaP substrate, as the used (002) reflection is very sensitive to anti-phase disorder.

3 MOVPE

In this thesis, the examined materials are grown using metal-organic vapor phase epitaxy (MOVPE). In addition to MOVPE, other epitaxial processes such as liquid phase epitaxy (LPE) and molecular beam epitaxy (MBE) exist. The advantages of MOVPE, however, are the wide availability of materials, and the possibility to grow very thin films. Additionally, it is possible to grow quantum dots with MOVPE.

MOVPE [59, 60] is an epitaxial growth process where the precursors are organometallic compounds and growth takes place from the gas phase. The layers can be grown at an atmospheric pressure or with a vacuum pump, a pressure lower than the atmospheric pressure. It is a major process in the growth of structures used in optoelectronics. In particular, blue light emitting diodes are manufactured using MOVPE. The growth rate depends on the temperature and the gas flows, but for example at a temperature of 700 °C the growth rate of gallium phosphide is about a micrometer per hour. The growth rate is slow enough to allow the precise control of thickness required for fabricating quantum wells.

The reactor can be a cold-wall reactor where only the susceptor is heated, so that the gases do not react before reaching the hot substrate sitting on the susceptor, or a hot-wall reactor where the entire reaction chamber is heated. The susceptor is made of a material that absorbs radiation well.

In this thesis, a Thomas Swan MOVPE reactor was used. It is a cold-wall reactor where the graphite susceptor is heated with a halogen lamp. The graphite susceptor is able to hold a 2 cm×2 cm substrate. The growth temperature is monitored with a thermocouple that is situated inside a glass tube in a hole in the susceptor. It should

be mentioned that all temperatures mentioned are thermocouple readings and thus the temperature of the sample surface is lower due to the fact that the flowing gases cool down the sample surface. The reactor walls consist of quartz glass and are cleaned periodically because of the tendency of the source materials to deposit on the reactor walls. All of the grown thin films were grown at an atmospheric pressure. The reactor that was used has a vacuum pump and therefore supports growth at a pressure lower than the atmospheric pressure, but the feature of growing at a pressure lower than the atmospheric pressure was not used. The used carrier gases were hydrogen and nitrogen. During growth, the hydrogen carrier gas was used and otherwise there is a constant nitrogen flow through the reactor.

The materials grown in this thesis consist of gallium, nitrogen, phosphorus and arsenic. The used precursors were trimethylgallium (TMGa), dimethylhydrazine (DMHy), tertiarybutylphosphine (TBP) and tertiarybutylarsine (TBAs). During growth, the TBP flow is turned on first and then the other precursors are introduced to the reaction chamber. The TBP flow is also turned off last. Having only a group V precursor does not result in layer growth, but prevents the evaporation of the group V atoms from the surface thus protecting the surface. The V/III ratio is about a hundred, so group III precursors are the ones that limit growth.

When the organometallic precursors are heated in the MOVPE reactor, they start to decompose in a reaction called pyrolysis. The pyrolysis is an extremely complex reaction, and there are also bimolecular reactions between the different precursors [61,62], so the exact pyrolysis reactions are not described here. It suffices to say that the bond between the grown element and the organic group is stronger the fewer carbon atoms there are in the organic group. Thus, for example triethylgallium decomposes faster at a low temperature when compared to trimethylgallium.

Because of the complexity of the reactions occurring, it is impossible to determine the composition of the layer accurately from gas flow ratios. This is especially true for group V precursors where at the used V/III ratios of about hundred an abundance of group V precursor molecules exist. Therefore it is important to have a separate method for determining the composition of grown layers. In the case of GaAsPN, the incorporation behaviour of group V elements has been extensively investigated [63].

4 Traditional measurement methods

This chapter describes the theory behind the traditional measurement methods AFM, XRR, HRXRD, PR and RBS. It should be noted that the theory presented here is not complete. If the reader wishes to get a complete understanding of these measurement methods, the references for AFM [64–71], XRR [72–75], XRD [22, 23], PR [76–79] and RBS [27, 28] are recommended.

4.1 Atomic force microscopy (AFM)

Atomic force microscopy (AFM) [64–71] is a type of scanning probe microscopy with a high resolution on the order of fractions of a nanometer. This is many orders of magnitude better than the diffraction limit of optical microscopes. The information of the sample surface is obtained by reflecting a laser beam from a cantilever to an array of four photodetectors. The relative detected intensity of the laser beam at the photodetectors gives information about the movement of the cantilever. The cantilever has a sharp tip at the end that is used to scan the sample surface. The sample holder can move the sample horizontally and vertically very accurately with a sub-nanometer precision. The principle of AFM is based between the forces of the sharp tip of the cantilever and the sample surface when the tip is brought close to the sample surface. AFM measurements can be performed in the contact mode where the deflection of the tip and thus the force between the tip and the sample

surface is maintained at a constant value, or in semicontact mode where the AFM tip oscillates at its resonant frequency and the forces between the sample surface and the tip act to modify the resonance frequency and the software adjusts the sample height to keep the oscillation frequency or amplitude constant.

In this thesis, an NT-MDT Ntegra Aura AFM was used. All of the atomic force micrographs have been taken in semicontact mode. The AFM is on top of a damped table to reduce vibrations originating from the environment.

4.2 X-ray reflectivity (XRR)

The refractive index for most materials at X-ray wavelengths is slightly smaller than one. Therefore, at low grazing angles of $\omega < 0.2^\circ$ a phenomenon called total external reflection (TER) is observed. At angles larger than this, the reflected intensity can be calculated from Fresnel equations. If there is a thin film on top of the substrate, interference effects as a function of angle can be seen. These interference effects allow determination of the thickness (via the spacing of the interference fringes) and electron density (via the strength of the interference fringes) of the thin film as long as there is a suitable electron density contrast between the substrate and the thin film. Additionally, if the surface of the sample is rough, a part of the reflected intensity goes to diffuse scattering, so the specular reflectivity intensity is lower. This effect allows the determination of the surface roughness. The most accurate analysis of the data is by fitting a theoretical simulated curve calculated from a layer model into the measured data. The determination of film thickness using XRR has been shown to have good inter-laboratory accuracy [80, 81]. For more information about XRR, see *e.g.* Ref. 72–75.

The main benefit of XRR for composition determination purposes is that it can be used to determine the electron density of a thin film, which is dependent on the composition of the film. However, the accuracy of electron density determination may not necessarily be high enough to be useful in composition determination of heteroepitaxial layers.

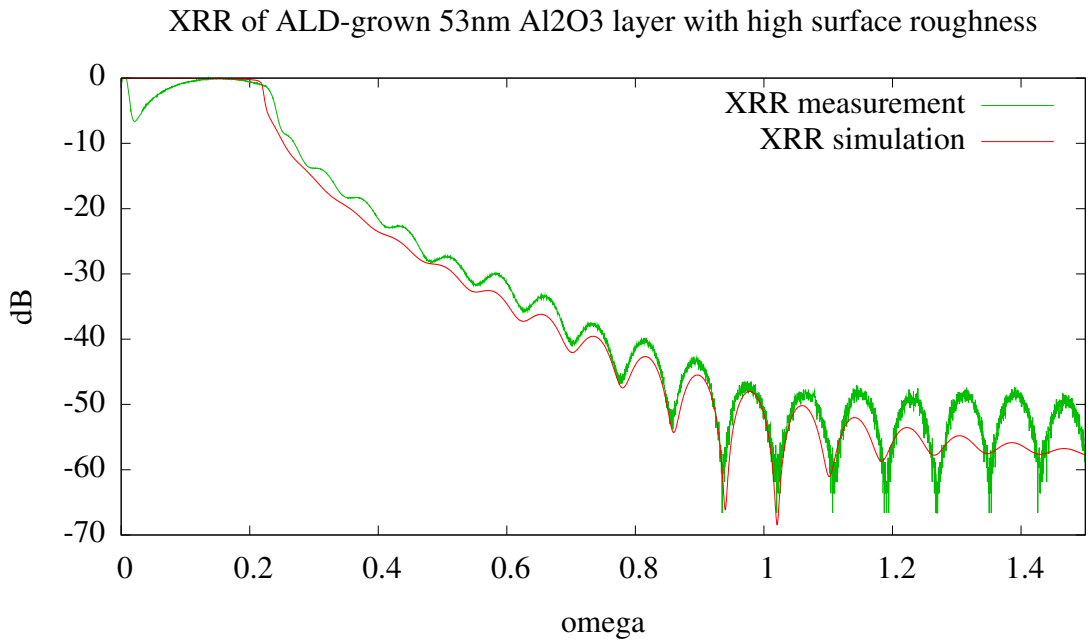

Figure 4.1: Example of simulated XRR curve fitted to measured data. The deviation between the measurement and the simulation at large angles is due to the non-Gaussian behaviour of the surface roughness factor [82].

In XRR measurements, an X-ray mirror, a 0.04 rad Soller slit, a 10 mm beam mask and a programmable divergence slit held at $1/32^{\circ}$ were used on the incident beam side. Additionally, a 0.1 mm copper attenuator was manually inserted and removed at the high-intensity regions of the reflectivity curve to achieve a linear response of the detector. At the reflected beam side, a thin film collimator, a 0.04 rad Soller slit and a flat graphite monochromator crystal were used. The detector used was a proportional counter. The XRR curves of the measurement were analyzed using a custom software, the algorithms of which have been reported previously [83, 84]. It should be noted that currently there exists free software for analyzing XRR measurements [85,86], which was not the case when the custom XRR software was written in 2006. Additionally, commercial software, some of which has

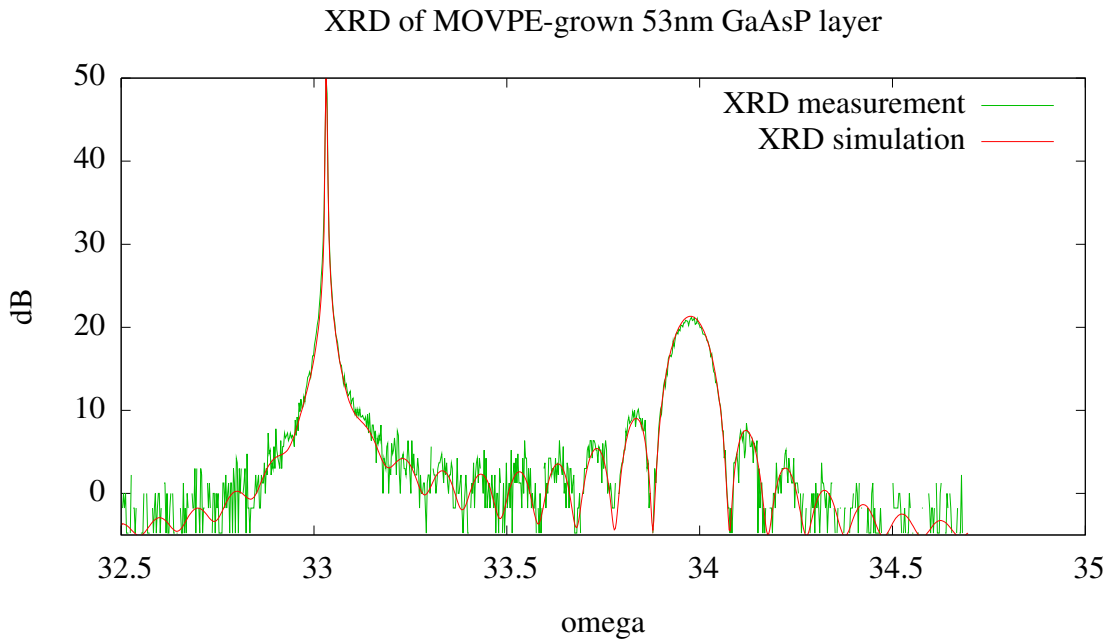

Figure 4.2: Example of simulated XRD curve fitted to measured data.

been described in the literature [87, 88], can also be used but such software often has high license costs. The custom software is based on Parratt's formalism [89] combined with the Névot-Croce interfacial roughness approximation [90].

4.3 High-resolution X-ray diffraction (HRXRD)

X-ray diffraction (XRD) [22, 23] is a phenomenon where the X-rays incident on a sample crystal diffract from the atoms of the crystal. As the atoms are ordered in a periodic crystal lattice, there exist directions where the interference of the waves scattered from the different atoms of the crystal is constructive. These directions can be calculated from Bragg's law.

With an X-ray diffractometer, it is possible to measure high-resolution scans of the diffraction intensity as a function of the angle. These high-resolution (HRXRD)

scans contain information not only about the lattice constants and thus the elemental compositions of the sample, but also interference fringes can be seen which contain information about the thickness of thin films. It has been shown that both XRR and XRD have good accuracy in thickness determination [91].

For samples of good enough quality, the sample can be modelled with a layer model consisting of a substrate and a number of homogeneous thin films on top of the substrate. With a fitting analysis, it is possible to obtain layer thicknesses and the distance between the diffracting planes along the direction of the diffraction vector, which can be used to calculate the lattice constant. By using Vegard's law [31,32], the composition of ternary semiconductors can be determined from the lattice constant.

If a good fit of the simulation model to the measurement cannot be obtained, it is still possible to obtain information about the lattice constant by using Bragg's law for the diffraction peak. *E.g.*, for a sample consisting of a substrate and a layer of poor crystalline quality, it is possible that a weak peak from the thin film can still be seen but the interference fringes that contain information about the layer thickness may be too weak to be distinguishable from background noise. In this case, it is possible to obtain the distance between the diffracting planes by using Bragg's law for the angle of the peak if the peak can be seen.

For symmetric reflections such as (004) for (001) oriented substrates, information is obtained for the lattice constant perpendicular to the surface of the sample.[1] For asymmetric reflections such as (113), the distance of the diffracting planes contains also information about the lattice constant parallel to the surface. Thus with the information from both a symmetric reflection and an asymmetric reflection, it is possible to determine the lattice constant parallel to the surface and to determine whether the layer is relaxed.

The XRD measurements were performed using a commercial Philips X-ray diffractometer with a four germanium (220) crystal monochromator and an X-ray mirror at the incident beam side and with an analyzer crystal at the diffracted

[1]...or nearly perpendicular, as all substrates are either intentionally or at least accidentally miscut a little bit.

beam side. The measurements were analyzed using a custom software that has been described previously [2]. Because the presented method depends on the values of crystal electric susceptibilities, it is important to note how they are calculated. In this case, the crystal electric susceptibilities were calculated with a method by Lugovskaya and Stepanov [92], using fitted sums of gaussian functions for atomic scattering factors [93] and tabulated values for dispersion corrections [94] and for Debye-Waller factors [95]. The curve itself was calculated with a recursive solution of the Takagi-Taupin equation [96] and differential evolution [97–100] was used as the fitting algorithm with a covariance-matrix based coordinate rotation during crossover [84]. Differential evolution in particular [101, 102] and genetic algorithms in general [103–105] have been previously applied to X-ray scattering curve fitting problems. The software does not support traditional optimization algorithms such as Levenberg-Marquardt [106, 107] or the simplex method [108] as they get stuck to false local optima. The global optimization algorithm simulated annealing [109, 110] is also not supported, as it requires too large calculation time in practice. Poisson's ratios and lattice constants were calculated with linear interpolation using Vegard's law [31, 32]. The software has been compared for the case of the samples analyzed in this thesis against Sergey Stepanov's X-ray server [111] at `http://x-server.gmca.aps.anl.gov/`, which uses a recursive matrix approach of dynamical XRD [112]. The simulated curves were almost identical, and thus the software can be trusted. Furthermore, a set of GaAsN samples previously analyzed with Philips' software [113] has been reanalyzed with the used software and the results have been found to be in good agreement [2].

4.4 Photoreflectance (PR)

PR is a measurement method for the differential change of the reflectance of a sample when another light source is illuminated on the sample surface [76–79]. The other light source is typically a laser, which is absorbed by the sample and the absorption of the illuminated light modifies the electric field near the sample surface. The electric

field causes a differential change in the reflectance of the sample. The differential change is especially large near photon energies corresponding to transitions between the valence band and the conduction band. Therefore PR allows determining these transitions, which can be used to make deductions about material composition.

Photoreflectance measurements can be performed in the bright configuration where the monochromator is placed between the sample and the detector, or in the dark configuration, where the monochromator is placed between the lamp and the sample. An advantage of the bright configuration is that laser scatter does not reach the detector and the luminescence of the sample reaches the detector only at the wavelength of the monochromator. In the bright configuration, the luminescence signal can be separately measured and subtracted from the combined luminescence and reflectance signal. In this work, bright configuration is used for that reason.

Information from photoreflectance signals can be performed by either manually determining the locations of the transitions from the features seen in the curve or alternatively with a fitting analysis. In this work, fitting analysis was used for samples #1–3.

The measurement apparatus has been manually built from standard laboratory equipment [114]. An Oriel Instruments halogen lamp is used as the light source. The power of the lamp can be adjusted by an adjustable Oriel Instruments constant-power supply. A power of 50 watts was used during the alignment of the components, and 250 watts was used during measurement.

All of the measurements were performed in a bright configuration where the monochromator was placed between the sample and the detector. The sample was attached with glue or with a two-sided adhesive tape to a copper coin, which is attached to a brass sample holder that can be rotated along the vertical axis. The temperature of the sample can be controlled with a compressor and a temperature-controlled heater element. However, all of the photoreflectance measurements here were performed in room temperature. A 405 nm InGaN laser diode was used which was temperature-controlled with a Peltier element to operate at 25 °C. The laser diode was powered by an adjustable constant current source and chopped with a chopper running at a known frequency, *e.g.* at 337 Hz. A Stanford Research Systems

lock-in amplifier was used to distinguish the PR signal at the chopper frequency from other signals. In some of the samples, PL was observed. The PL signal was measured by turning off the halogen lamp and subtracted from the combined PL and PR signal measured with the halogen lamp on. For PR measurement procedures, see Appendix 4.

4.5 Rutherford backscattering spectroscopy (RBS)

Rutherford backscattering spectroscopy (RBS) [27,28] is an analytical technique that utilizes the backscattering of typically alpha particles to obtain information about the sample. An RBS instrument consists of three components: an ion source that gives a beam of usually alpha particles, a linear particle accelerator to accelerate the ions to high energies, typically to the range 1–3 MeV, and a detector that is capable of measuring the energies of backscattered ions over a range of angles.

The energy for the backscattered particles can be obtained by considering the kinematics of the collision, namely the conservation of momentum and energy, and thus the energy of a backscattered particle gives information about the mass of the atom into which the particle collided. To obtain composition information, an equation of the probability of the backscattering event is also required.

Because particles travelling in a material slow down gradually, RBS is a surface-sensitive technique and is capable of determining the layer thickness accurately.

RBS can be combined with nuclear reaction analysis (NRA). In this case, the ion beam causes nuclear reactions in certain atoms such as nitrogen. The radiation emitted by these nuclear reactions is detected, and with a suitable standard the absolute composition of certain atoms can be calculated. This technique is especially useful for detecting the nitrogen content in dilute nitrides, as the nitrogen content is typically very small and hard to detect with RBS alone. For RBS/NRA measurement procedures, see Appendix 3.

5 Novel measurement methods

This chapter describes the related theory behind the developed measurement methods. First, how the PR composition determination method works for GaAsPN is demonstrated in Section 5.1. Then, in Section 5.2 how the composition affects different variables in X-ray scattering curves is analyzed and it is demonstrated that a measurement method based on the location and intensity of (002) XRD peak looks promising, as does a measurement method based on the location of an XRD peak and XRR-determined electron density. Furthermore, the potential error sources affecting the (002) XRD measurement method and the XRR-determined electron density are identified and a procedure for doing the fitting analysis for the (002) XRD measurement method is described, as is a procedure for determining material composition from XRR-determined electron density and XRD-determined lattice constant. Additionally, in Section 5.3, a novel method is described for testing whether an epilayer is fully strained.

5.1 PR composition determination

The PR composition determination method is based on determining the energies of the transitions from the valence band to the split conduction band. The transition energies are dependent on the material composition, and a model which tells what these transition energies as a function of composition are can be inverted to detremine the composition as a function of the transition energies. Because there are two transitions between the valence band and the conduction band split into two,

with the knowledge of these transition energies the full composition of a quaternary material can be determined.

The band anticrossing model predicts that the conduction band splits into two [3, 4]

$$E_{\pm}(k) = \frac{1}{2}[(E_{M\Gamma}(k) + E_N) \pm \sqrt{(E_{M\Gamma}(k) - E_N)^2 + 4xC_{NM}^2}], \tag{5.1}$$

where the minimum of the conduction band at the Γ band edge of $GaAs_yP_{1-y}$ is calculated from Equation 2.1 and linear interpolation is used for the nitrogen level E_N (1.65 eV for GaAsN and 2.18 eV for GaPN) and the coupling parameter C_{NM} (2.7 eV for GaAsN and 3.05 eV for GaPN).

Here it should be noted that the usage of the BAC model has often been criticized by theorists as it fails to take into account the impacts of all different N configurations to the material band structure [115, 116]. It can be speculated that with a model more accurate than the BAC model, the PR composition determination could be made more accurate.

Solving the values of x and y from the nonlinear system of equations is not possible with algebraic means. Therefore, a computer program to solve the equation using numerical algorithms was written using GNU Octave (see Appendix 2). This program can be used to determine the composition of a quaternary material when the transition energies from the photoreflectance measurement are known. The transition energies can either be determined manually or ideally with a fitting analysis.

5.2 X-ray based composition determination

5.2.1 Introduction

Both HRXRD and XRR measurements are sensitive to the composition of a thin film, but in different ways: in XRR measurements the composition of the thin film affects its electron density whereas in XRD measurements the composition of the thin film affects the unstrained lattice constant of the thin film.

In XRR measurements, the composition of the thin film affects its electron density, which can be measured with a curve-fitting analysis from the measured data. The accuracy of XRR has been previously studied and it has been found that the relative accuracy of mass density determination is about 3%, but that is for ALD-grown aluminium oxide on top of silicon [117, 118]. If this is the case, it is unlikely that this accuracy would be good enough for determining the layer composition accurately.

In HRXRD, the composition affects the unstrained lattice constant according to Vegard's law [31, 32]. Below the critical thickness, the lattice constant of an epitaxially grown thin film parallel to the surface is forced to the same value as the lattice constant of the substrate. Perpendicular to the surface, the value of the lattice constant can be calculated from Poisson's ratio and lateral strain. Of these two different composition measurements methods (XRR and HRXRD), HRXRD is significantly more accurate but works only for crystalline materials and therefore HRXRD is the main X-ray technique for measuring composition of heteroepitaxial semiconductors. Another advantage of HRXRD is that for thin films of poor crystalline quality, the position of the peak is not changed although the peak may become weaker. Even if fitting analysis is impossible, it is still possible to determine the lattice constant using Bragg's law.

With only one measured real variable, only one free composition variable in the sample model can be fitted to the measured data. Thus for quaternary semiconductors of the type $A_xB_{1-x}C_yD_{1-y}$ or $AB_xC_yD_{1-x-y}$ determining both x and y from a single X-ray curve using traditional methods is not possible.

Determining the composition of a quaternary semiconductor needs two different composition related variables. The variables can for example be:

1. Location of the Bragg peak in XRD
2. Intensity of the Bragg peak in XRD
3. Electron density in XRR

Unfortunately, small changes in composition result in small changes in intensity

of the Bragg peak for the usually used (004) reflection in XRD measurements. It is unlikely that this variable could be determined accurately enough.

In this section, two X-ray based composition determination methods are described. The first method uses the location and intensity of the (002) XRD Bragg peak. The second method uses the location of the (004) XRD Bragg peak and the electron density as determined by XRR.

5.2.2 XRD peak intensity and location based method

5.2.2.1 Introduction

The intensity of a reflection can be calculated from the structure factor, which takes into account interference effects from the reflecting waves coming from all atoms within the unit cell. Some reflections are called quasi-forbidden reflections. In these reflections such as (002) for zinc-blende semiconductors, destructive interference reduces the intensity of the reflection. As the III and V atoms have a different reflection coefficient, the destructive interference does not totally eliminate all of the intensity of the reflection and thus a weak reflection can be seen. Due to the partial destructive interference, the intensity of these quasi-forbidden reflections is more sensitive to the composition of the material than *e.g.* the (004) reflection. In particular, the intensity of a quasi-forbidden (002) reflection has been shown to depend strongly on the composition of the ternary $Al_xGa_{1-x}P$ and quaternary $In_xAl_{1-x}As_ySb_{1-y}$, allowing the use of the intensity of the reflection as a second free variable in composition determination, which makes it possible to determine the composition of a quaternary material with a single X-ray scan. [119, 120]

To investigate the feasibility of using the (002) reflection intensity to determine the composition of $GaAs_yP_{1-x-y}N_x$, several curves were simulated for the (002) and (004) reflections with varying values of y and with x set so that the lattice constant of the material stays the same. The simulated curves are shown in Figures 5.1(a) and 5.1(b). Note that the some of the simulated curves in the figures are clearly unphysical, *e.g.* it is assumed that the layers are fully strained and the nitrogen

content x to keep the lattice constant the same was unrealistically large from the fabrication point of view in some cases. The figures are only meant to illustrate how the intensity of the peak varies as a function of the As content y. It can be seen that the intensity of the (004) peak is practically independent of the As content while the intensity of the quasi-forbidden (002) reflection varies strongly with the As content, making it potentially possible to determine the composition of a quaternary semiconductor by taking into account the intensity of the peak in addition to the location of the peak. In this work, the intensity and the location of the quasi-forbidden (002) reflection are used to determine the composition of GaAsPN layers.

5.2.2.2 Error sources

Use of the peak intensity is not as accurate as peak position in determining the composition of the material. In particular, the following sources of error may be present:

- Poisson-distributed photon counting noise and other measurement related inaccuracies such as sample misalignment. This can result in either too high or too low determined arsenic content. This error source is random and can be reduced by making the measurement multiple times in the case of sample misalignment and using longer photon counting times in the case of photon counting noise. The magnitude of these measurement related inaccuracies can be estimated by making the measurement multiple times and doing fitting analysis for each measurement separately.

- The crystal planes of the epilayer may be tilted differently from the substrate. For example, it has been shown that a GaP layer grown on a misoriented silicon surface relieves the strain energy by tilting the crystal planes [121]. If this is the case, the true thin film peak may be at a different ω or Ψ angle than the peak of the substrate. Note here that alignment is typically done for the substrate peak. The result is that the peak observed in a 1-axis $\omega - 2\theta$ scan is

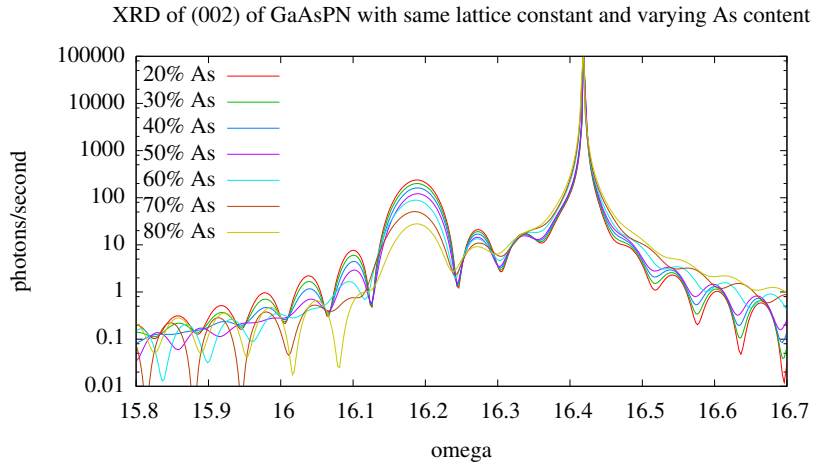

(a)

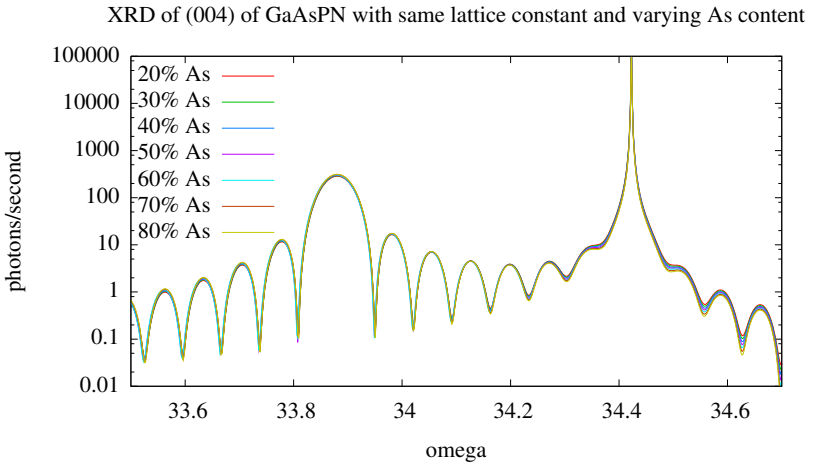

(b)

Figure 5.1: Simulated XRD curves for the (a) quasi-forbidden (002) reflection and (b) allowed (004) reflection of a 75 nm thick $GaAs_yP_{1-x-y}N_x$ with varying values of y and with x set so that the lattice constant stays the same. Note that some of the simulated curves are unphysical, *e.g.* the layer was assumed to be fully strained which might not be true in reality and the N content x was unrealistically large for some layers.

weaker than the true peak. The result is that the determined arsenic content is too high, as both an increased arsenic content and tilting of the crystal planes result in a weaker peak. With a reciprocal space map of a symmetric reflection (or ideally two, one at $\phi = 0^\circ$ and another at $\phi = 90^\circ$) it can be checked that the true thin film peak occurs at the same ω angle as the observed thin film peak. Additionally, with ω and Ψ scans the same check can be done but in a significantly faster way.

- The epilayer may have degraded crystal quality. For example, nitrogen related point defects may be present in the case of GaAsPN. Typically in dilute nitrides, nitrogen is not fully substitutionally incorporated into the crystal lattice. The different possible nitrogen configurations may cause strain fields around them, affecting the reflection intensity. Due to degraded crystal quality, the peak will become weaker, which results in too high determined arsenic content.

- The layer may be partially relaxed. If this is the case, this results in a determined nitrogen content that is too high, as both relaxation and an increase in nitrogen content tend to move the peak to a higher θ angle without materially affecting the peak intensity. However, it should be noted that strain relaxation is associated typically with degraded crystal quality, so the determined arsenic content will typically also be too high if the layer is relaxed. The relaxation may be studied with reciprocal space maps of asymmetric reflections or with the method presented in Section 5.3 and can be eliminated by ensuring that the layer thickness is below the critical thickness for strain relaxation.

- The atomic scattering factors used to calculate crystal electric susceptibilities may be inaccurate. If they are slightly incorrect, the effect of the peak intensity varying with material composition is seen, but the magnitude of the effect in simulations will deviate from the magnitude in real measurements. Thus, the determined arsenic content will be off.

Additionally, it should be noted here that the lattice constant is determined very accurately by a high-resolution X-ray diffractometer, whereas the peak intensity will not be as accurate as lattice constant in determining material composition. Thus, the determined arsenic and nitrogen contents have a crosserror: if *e.g.* the determined arsenic content is too high due to one of the mentioned error mechanisms, this would move the peak to a lower θ angle without an associated increase in nitrogen content. However, the location of the peak is very accurately known and stays fixed, as the previously mentioned error mechanisms affect mainly only the peak intensity and not its location[1]. Therefore, the determined too high arsenic content will lead to a determined nitrogen content that is also too high.

It should also be noted that although the determined lattice constant is very accurate, Vegard's law [31, 32] may not be true for dilute nitrides. For example, it has been observed that the lattice constant of InAsN deviates significantly from Vegard's law due to non-substitutional incorporation of nitrogen into the crystal lattice [122]. Additionally, for GaPN it has been incorrectly determined with XRD that the nitrogen content is 0.02 while the real nitrogen content was 0.036, which was explained also by non-substitutional incorporation of nitrogen into the crystal lattice [123]. In the work, the substitutional nitrogen content is 0.024 which is closer to the XRD-determined nitrogen content of 0.02. The accuracy of Vegard's law has also been investigated for InGaN [124] and InGaAsP [125], and it has been observed that there is a deviation from Vegard's law.

In summary, the systematic error sources cause the peak to become weaker and the determined arsenic content (crystal quality issues) or the nitrogen content (relaxation) in being too high, while the random photon counting noise error source can either result in too high or too low arsenic content. There is crosserror between the determined nitrogen and the arsenic content: if due to crystal quality issues the determined arsenic content is too high, it causes the determined nitrogen content to also be too high. An estimate for the photon counting noise can be obtained by performing the measurement twice and seeing how the determined arsenic content

[1]with the exception of strain relaxation which affects also peak location

values differ. The amount of systematic error cannot be estimated in this way.

5.2.2.3 XRD peak intensity and location fitting analysis

To determine if the composition of the samples could be determined with XRD alone, a simulated curve with a fixed trial As content is fitted into the measured curve. The fitting error values of the function used in the fitting analysis were then plotted as a function of the trial As content. The determined As content is at the minimum of the fitting error function curve. The N content and the layer thickness is obtained from the fitting analysis at the minimum of the curve. The software used doesn't support determining the composition of a quaternary semicondutor, but as it exposes the value of the fitting error function used in the fitting analysis to the user, it is possible to fit one composition parameter and manually determine the minimum of the fitting error as a function of the other composition parameter.

The fitting analysis here is somewhat different than but similar to the the integration method used previously to determine the composition of $In_xAl_{1-x}As_ySb_{1-y}$. [120] As the method here is based on a fitting analysis, the method takes into account the intensity of the whole peak, not just its maximum, and is therefore similar to the integration method. Normalization is achieved by using the normalization constant as one fitting parameter, which results in the simulated and measured curves in being at the same height in logarithmic scale. The method presented here would be easier to implement in a curve-fitting software than the integration method, as the only change needed would be to simply allow the fitting of another composition-related parameter, which would eliminate the manual minimum determination step in the method.

To investigate if the fitting error function has an effect on the determined composition, four different fitting error functions are used. The first fitting error function that takes into account the Poisson-distributed photon counting noise in a correct way is

$$F_1 = \chi^2 = \sum \frac{(P_{\text{meas}} - P_{\text{simul}})^2}{P_{\text{meas}}}, \tag{5.2}$$

where P_{meas} and P_{simul} are the measured and simulated photon counts, respectively.

Note that as the standard deviation of photon counting noise is the square root of the measured photon count, the numerator contains the difference squared and the denominator contains the standard deviation squared. Thus the difference is divided by its standard deviation and a square is taken of the result. Unfortunately the χ^2 fitting error function gives too much weight to the Bragg peak of the GaP substrate in comparison to the GaAsPN layer. This is a significant problem, as in the analysis it is assumed that the only source of error is Poisson noise. In reality, the used simulation model might not reproduce the shape of the substrate peak accurately enough. Additionally, the used X-ray detector can have a nonlinear response at high intensities. Therefore, the fitting error function χ^2 needs modifications in order to be useful.

The second used fitting error function was mixed relative/χ^2 which is the same as χ^2 below a critical photon rate C and proportional to the relative error above a critical photon rate. The function is the sum of:

$$F_2 = \begin{cases} \sum \frac{(p_{\text{meas}} - p_{\text{simul}})^2}{p_{\text{meas}}}, & p_{\text{meas}} < C \\ \sum \frac{(p_{\text{meas}} - p_{\text{simul}})^2}{p_{\text{meas}}^2 / C}, & p_{\text{meas}} \geq C \end{cases}, \tag{5.3}$$

where p_{meas} and p_{simul} are the measured and simulated photon *rates*, respectively, measured in photons/second and the parameter C was set to 100 photons/second to prevent the Bragg peak from having too much weight. The third was 1-norm in logarithmic space:

$$F_3 = \sum |\log p_{\text{meas}} - \log p_{\text{simul}}|, \tag{5.4}$$

and the fourth was 2-norm in logarithmic space:

$$F_4 = \sqrt{\sum (\log p_{\text{meas}} - \log p_{\text{simul}})^2}. \tag{5.5}$$

5.2.3 XRD peak location and XRR electron density based method

5.2.3.1 Introduction

If XRR electron density could be determined accurately enough, it could be used as a second composition dependent variable in addition to the XRD peak location. It has been previously demonstrated [117, 118] that the accuracy of density determination in XRR is 3.5%. The accuracy is low because of Poisson-distributed photon counting noise. However, this low accuracy is caused by the fact that an extended fitting range is used and the used fitting error function is 2-norm in logarithmic space. The first article [117] demonstrated that with a suitably designed fitting error function, one can determine mass density much more accurately. Additionally, tests have been performed and it was found out that restricting the end of the fitting range to a region where photon counting noise is not so prevalent also improves density determination accuracy. In this thesis, two methods to avoid low accuracy are used:

1. The end of the fitting range is restricted to 1°. Actually, this would be necessary for other reasons too in addition to avoiding photon counting noise: after 1° the simulation no longer matches the measurement due to non-Gaussian behaviour of the surface roughness factor [82].

2. The fitting error function used is mixed relative/χ^2 instead of the more commonly used 2-norm in logarithmic space.

For XRR analysis, mixed relative/χ^2 fitting error function is defined as

$$F_2 = \begin{cases} \sum \frac{(r_{\text{meas}} - r_{\text{simul}})^2}{r_{\text{meas}}}, & r_{\text{meas}} < C \\ \sum \frac{(r_{\text{meas}} - r_{\text{simul}})^2}{r_{\text{meas}}^2 / C}, & r_{\text{meas}} \geq C \end{cases}, \tag{5.6}$$

where r_{simul} and r_{meas} are the simulated and measured reflectivities and C is a free parameter for which the value of 0.001 is used for XRR measurements. Note that the definition of the fitting error function is the same as for XRD analysis with the

exception that reflectivities are used instead of photon rates and the value of C is 0.001 instead of 100 photons/second.

There are two possible ways how to determine material composition based on XRD and XRR scans. One possibility, the most ideal way, is to fit XRD and XRR curves simultaneously. However, that requires software that is designed to fit both XRD and XRR curves. The software used consisted of two individual components that do not work together. A slightly less ideal way to determine the material composition is to determine the electron density from XRR measurement and then use various trial As and N contents to calculate a theoretical electron density to see which trial contents give the correct electron density. The trial As and N contents are linked together: when a trial As content is selected, XRD fitting analysis is performed to fit the location of the XRD peak giving the trial N content which explains the location of the XRD peak together with the trial As content.

In order to calculate the electron density, the mass density of the layer needs to be known first. For $GaAs_yP_{1-x-y}N_x$, the mass density is

$$\rho = \frac{4m_{\mathrm{Ga}} + 4ym_{\mathrm{As}} + 4(1-x-y)m_{\mathrm{P}} + 4xm_{\mathrm{N}}}{a_{\parallel}a_{\parallel}a_{\perp}}, \tag{5.7}$$

where $a_{\parallel}$ is the lattice constant of the thin film parallel to the surface, $a_{\perp}$ is the lattice constant of the thin film perpendicular to the surface and determined from XRD (004) scan via curve fitting analysis, m_{X} for X = Ga, As, P and N is the mass of the atom in kilograms and y and x are the As and N contents.

When the mass density is known, the electron density can be calculated from

$$\rho_e = \frac{f_{\mathrm{Ga}} + yf_{\mathrm{As}} + (1-x-y)f_{\mathrm{P}} + xf_{\mathrm{N}}}{m_{\mathrm{Ga}} + ym_{\mathrm{As}} + (1-x-y)m_{\mathrm{P}} + xm_{\mathrm{N}}}\rho \tag{5.8}$$

where y and x are the As and N contents, m_{X} is the atomic mass of X = Ga, As, P and N in kilograms and $f_{\mathrm{X}} = Z_{\mathrm{X}} + \Delta f'_{\mathrm{X}}$ is the atomic scattering factor of X = Ga, As, P and N where Z_{X} is the atomic number and $\Delta f'_{\mathrm{X}}$ is the Hönl anomalous dispersion correction real part tabulated *e.g.* in Ref. 94. Finally, note that ρ_e is not the real density of electrons in the material. It is the density of electrons that

would explain the optical properties of the material if electrons behaved ideally. The inclusion of the Hönl anomalous dispersion correction takes into account the non-ideal behaviour of electrons. For a GNU Octave function to calculate the electron density of GaAsPN and its usage instructions, see Appendix 5.

The XRR curve fitting software should be able to calculate ρ_e based on the fitted layer mass density. Typically the fitting parameter is the mass density and not the electron density, but as they are linearly related to each other, it is possible to determine the electron density by using a trial composition to fit the mass density and then calculate the electron density. The determined electron density should be relatively independent on the trial composition but the determined mass density is obviously dependent on the trial composition. If the XRR curve fitting software does not expose the value of electron density to the user, Eq. 5.8 can be used to calculate the electron density from the mass density and the trial composition.

5.2.3.2 Error sources

There are at least a few error sources which may affect the XRR-determined electron density:

1. It is possible that the sample is misaligned and thus the critical angle is determined incorrectly [126]

2. It is possible that the oscillation amplitude of the interference fringes is different in the measurement when compared to the simulation. For example, it has been speculated that the Névot-Croce interfacial roughness model causes artificially strong interference fringes in the simulation [127].

3. Poisson-distributed photon counting noise also affects the determination of electron density, especially so if the 2-norm in logarithmic space fitting error function is used and if the fitting range is extended to the noisy region. This error source has been investigated previously [117, 118], but the investigations are incomplete: for example, these investigations have not researched what

effect reducing the fitting range far away from the noisy region has on the material parameter determination accuracy.

4. When the electron density is calculated from the mass density, Hönl anomalous dispersion corrections need to be used. It is possible that these anomalous dispersion corrections have incorrect values. The values tabulated in Ref. 94 are used in this work, but it is by no means certain that they are accurate.

In this work, the second and third error sources are reduced by using the mixed relative/χ^2 fitting error function and restricting the end of the fitting range to 1°. This causes the electron density determination to use the critical angle region and the very first interference fringes, which are the most accurately determined ones.

Additionally, it should be noted that the lattice constant is determined very accurately by a high-resolution X-ray diffractometer, but the electron density determination by XRR is inaccurate *e.g.* due to possible sample misalignment. If the XRR determined electron density gives a too high arsenic content, this would move the peak to a lower θ angle without an associated increase in nitrogen content. However, the location of the peak is very accurately known and stays fixed, as the XRD error mechanisms affect mainly only the peak intensity and not its location[2]. Therefore, the determined too high arsenic content will lead to a determined nitrogen content that is also too high.

5.3 Novel relaxation test method

5.3.1 Introduction

Some commercial software have the capability to determine strain state based on fitting multiple XRD ω-2θ scans at the same time, some from an asymmetric reflection such as (113) and some from a symmetric reflection such as (004). For example, for PANalytical Epitaxy, a set of four ω-2θ scans is recommended for most

[2]with the exception of strain relaxation which affects also peak location

accurately determining the strain state. The software automatically compensates away the effect of crystal plane tilt when four ω-2θ scans are used. However, the used custom software has no such support. To determine whether the layers are fully strained, a novel manual method for performing a relaxation check with a triple-crystal diffractometer was developed in this thesis. The method is based on comparing the location of the (113) XRD peak to the theoretically predicted value of a fully strained film.

Another way to determine whether the layers are fully strained is to acquire a RSM of the (113) reflection and seeing whether the thin film peak occurs at the same value of the diffraction vector component along the crystal plane as the substrate peak. However, the drawback of RSMs is the slow data acquisition time. An advantage of RSMs here is that they are able to find evidence of a strain gradient. For example, it has been shown that InGaN may have a strain gradient [128].

5.3.2 Mathematical background

It should be noted that due to the tetragonal distortion of the unit cell, the crystal planes of the asymmetric reflections in the thin film have an offset angle different from the substrate even though the crystal planes parallel to the surface have not been tilted. This is illustrated in Figure 5.2. The angle difference can be calculated from the dot product of the reciprocal lattice vectors of the substrate and the thin film and for the (113) reflection is

$$\alpha = \arccos \frac{\frac{1^2}{a_s a_\parallel} + \frac{1^2}{a_s a_\parallel} + \frac{3^2}{a_s a_\perp}}{\sqrt{(\frac{1}{a_s})^2 + (\frac{1}{a_s})^2 + (\frac{3}{a_s})^2}\sqrt{(\frac{1}{a_\parallel})^2 + (\frac{1}{a_\parallel})^2 + (\frac{3}{a_\perp})^2}} \tag{5.9}$$

where a_s is the lattice constant of the substrate, $a_\parallel$ the lattice constant of the thin film parallel to the surface and $a_\perp$ the lattice constant of the thin film perpendicular to the surface. Here $a_\perp$ was calculated from Bragg's law of a symmetric reflection. As we assume a fully strained film, $a_\parallel = a_s$. Here for gallium phosphide $a_\parallel = a_s = 5.4505$ Å. Note that the previous equation loses sign information and gives always

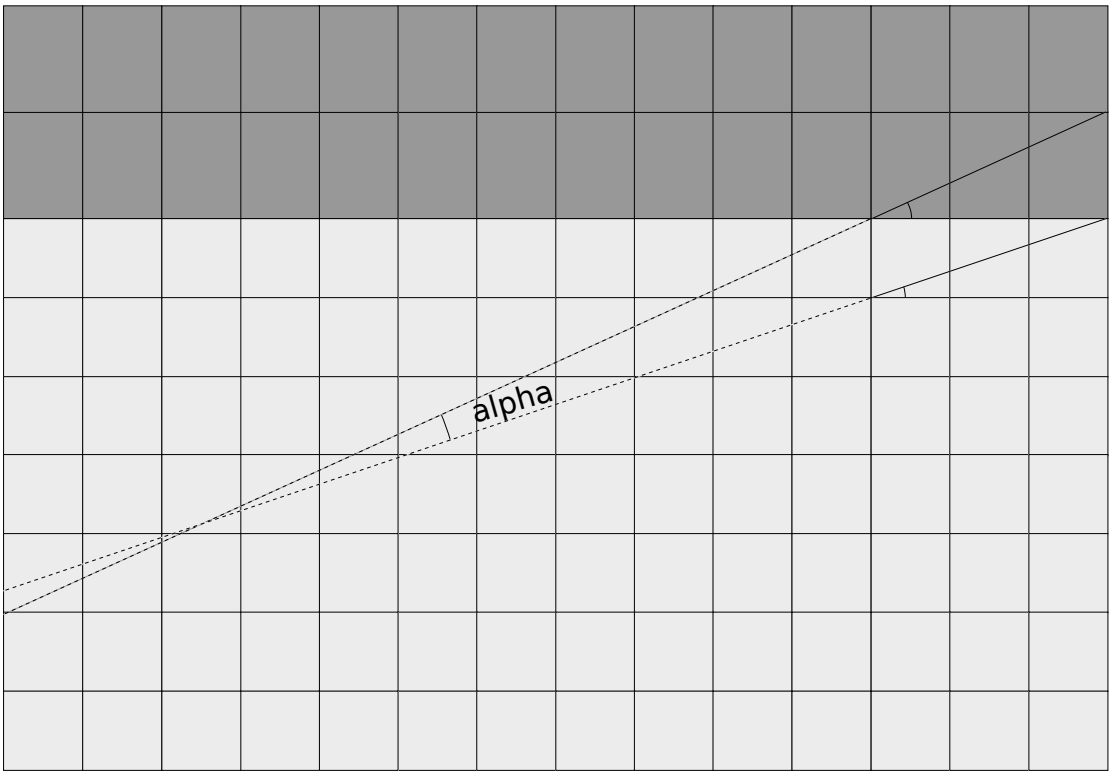

Figure 5.2: Tetragonal distortion of the unit cell changes the offset angle of the thin film to a different value than the offset angle of the substrate.

positive offset angle difference. The sign needs to be inverted to be negative if $a_\perp$ is smaller than $a_\parallel$.

The predicted location of the peak can be calculated using Bragg's law and the interplanar distance of the reflecting planes d_{113} where

$$d_{113} = \frac{1}{\sqrt{(\frac{1}{a_\parallel})^2 + (\frac{1}{a_\parallel})^2 + (\frac{3}{a_\perp})^2}}, \tag{5.10}$$

where $a_\parallel$ and $a_\perp$ are defined as previously and

$$\theta_{113} = \arcsin \frac{\lambda}{2d_{113}}, \tag{5.11}$$

where λ is the wavelength of the used X-rays. These equations can be used to calculate the location of the substrate XRD peak if a_s is substituted for $a_\parallel$ and $a_\perp$.

The $\omega - \theta$ offset angle for the (113) reflection of (001) oriented substrates is theoretically

$$\omega - \theta = \beta_{(113)} = \arctan \frac{\sqrt{1^2 + 1^2}}{3}, \tag{5.12}$$

however, the miscut of the substrate modifies the actual angle so the previous equation calculates only an initial guess and the real offset angle needs to be found with a diffractometer.

If the peak can be seen with the predicted $\theta - \omega$ offset angle with the difference α from the $\theta - \omega$ offset angle of the substrate peak and occurs with the predicted θ angle calculated from d_{113}, it can be concluded that the layer is fully strained. However, it should be noted that this presented method does not work perfectly when there are strain gradients in the thin film.

In order to calculate the approximate in-plane lattice constant of the thin film, the reciprocal lattice vector component parallel to the (001) planes needs to be known. For (113) reflections on (001) substrates it is [129]

$$H_\parallel = \frac{1}{\lambda}(\cos(2\theta_{(113)} - \omega'_{(113)}) - \cos(\omega'_{(113)})), \tag{5.13}$$

where $\omega'_{(113)} = \theta_{(113)} + \beta_{(113)} + \alpha$ is the angle of incidence measured from the (001) planes, $\theta_{(113)}$ is the diffraction angle and λ is the wavelength of the used X-rays.

After $H_\parallel$ has been calculated for the observed peak, it is possible to calculate the approximate in-plane lattice constant from

$$a_\parallel = \frac{\sqrt{1^2 + 1^2}}{H_\parallel}, \tag{5.14}$$

which is valid for (113) reflection on (001) cut substrates. It should be, however, noted that the equation is only very approximate as the true peak in the ($H_{\parallel}$, $H_{\perp}$) reciprocal space may not be paraxial, so for relaxed layers the true maximum of the peak may occur at a different $H_{\parallel}$ value than the peak observed in a 1-dimensional ω-2θ scan.

The degree of relaxation of a layer is defined as

$$R = 1 - \frac{a_{\parallel} - a_0}{a_s - a_0}, \tag{5.15}$$

where a_s is the substrate lattice constant, a_0 is the strain-free thin film lattice constant and $a_{\parallel}$ is the true in-plane lattice constant of the thin film. According to the definition of degree of relaxation, $R = 1$ if $a_{\parallel} = a_0$ and $R = 0$ if $a_{\parallel} = a_s$, so the definition makes sense.

Finally, the strain-free lattice constant a_0 can be calculated from

$$a_0 = \frac{(1 - \nu)a_{\perp} + 2\nu a_{\parallel}}{1 + \nu}, \tag{5.16}$$

where $a_{\perp}$ and $a_{\parallel}$ are defined as previously and ν is the Poisson's ratio for the thin film. For GaAsP and GaAsPN, the value 0.309 which is halfway between the values for GaP (0.307) and GaAs (0.311) can be used. For GaPN, the value for GaP (0.307) should be used.

5.3.3 Method application

The novel method to determine the strain state of a layer proceeds as follows:

1. A symmetric ω-2θ scan such as (004) scan for (001) cut substrates needs to be acquired.

2. The strained out-of-plane lattice constant is determined from the layer symmetric peak location and Bragg's law.

3. The diffractometer is aligned to the symmetric thin film peak and it is verified

with ω and Ψ scans that the layer peak occurs for the same $\omega - \theta$ offset and tilt angle Ψ as the substrate peak. If this is not the case, the layer crystal planes are tilted differently from the substrate and the relaxation check cannot be trusted.

4. The substrate (113) peak location is calculated using Eq. 5.10 (substituting a_s for $a_\parallel$ and $a_\perp$) and Eq. 5.11. The $\omega - \theta$ offset angle of the substrate (113) peak is calculated using Eq. 5.12. The diffractometer is aligned to the substrate peak by enterng the calculated θ and $\omega - \theta$ offset values. The sample rotation angle Φ is adjusted so that the peak is seen and standard diffractometer alignment procedures are used afterwards (see Appendix 1).

5. The $\omega - \theta$ offset difference between the thin film and the substrate are calculated from Eq. 5.9. Note also that the sign of α needs to be modified to be negative if $a_\perp$ is smaller than $a_\parallel$. The predicted thin film peak location is also calculated from Eq. 5.10 and Eq. 5.11.

6. The $\omega - \theta$ offset angle the diffractometer is aligned to is modified by adding to it the calculated offset angle difference α. Note that the sign of α must be changed to be negative in some cases. The diffractometer is aligned to the predicted thin film peak location θ.

7. If the thin film peak is seen at the predicted θ location, the layer is fully strained. If not, the layer is at least partially relaxed.

6 Results and discussion

The chapter is organized in the following way: Section 6.1 presents the description of the grown samples. Section 6.2 presents the structural and composition characterization of the samples with the results of AFM and RBS/NRA measurements. Section 6.3 contains the results of the PR measurements and the comparison of PR measurements with RBS/NRA measurements and XRD peak location. In Section 6.4, it is verified with the novel method that samples #1–5 are fully strained. In Section 6.5, the full quaternary composition of the layers is determined from the (002) XRD scan and the accuracy of the method is improved by taking into account the weakness of the (004) XRD peak. Finally, in Section 6.6, the full quaternary composition of the layers is determined from the (004) XRD scan and the XRR-determined electron density.

6.1 Samples

GaAsPN layers were grown on GaP substrates using MOVPE as the fabrication method. The used growth parameters and sample information is listed in Table 6.1.

The 20 nm thick GaAsPN layer in sample #0 was grown on top of a 70 nm gallium phosphide buffer layer and the gallium phosphide substrate. The 30 nm and 130 nm thick GaAsPN layers #1–9 were grown directly on top of the GaP substrate. Three samples #1–3 were grown with slightly varying DMHy/V ratios and TBAs/V ratios. Samples #4–5 were grown with TBAs/V ratios that were very small and zero. The samples #6–9 are similar to samples #5, #4, #1 and #2,

Table 6.1: Grown GaAsPN samples. All samples were grown at a temperature of 600 °C and were subsequently annealed for 5 minutes at 750 °C.

Sample	thickness	buffer	V/III	DMHy/V	TBAs/V
#0	20 nm	70 nm	100	0.32	0.045
#1	30 nm	no	101	0.32	0.045
#2	30 nm	no	103	0.32	0.061
#3	30 nm	no	106	0.39	0.054
#4	30 nm	no	100	0.30	0.020
#5	30 nm	no	98	0.31	0.000
#6	130 nm	no	101	0.32	0.000
#7	130 nm	no	103	0.32	0.020
#8	130 nm	no	101	0.32	0.046
#9	130 nm	no	103	0.32	0.061

respectively, but are 130 nm thick. The samples most suitable for XRD analysis are the 30 nm thick samples. The 130 nm thick set of samples was grown with similar DMHy/V and TBAs/V ratios as some of the 30 nm thick samples in order to be able to deduce the N content with NRA measurements, as the NRA measurements were not successful for the 30 nm thick samples.

6.2 Structural and composition characterization using established methods

The surface morphology of the samples was studied by atomic force microscopy. Ideally, the roughness of the surface should be as low as possible and there should be no holes. Atomic steps should be clearly visible. The surface quality is important because the models used in XRR and XRD fitting analysis assume that the surface has good quality.

The surface of the sample #0 was investigated using an atomic force microscope. It was determined that the height variations of the surface were on the order of

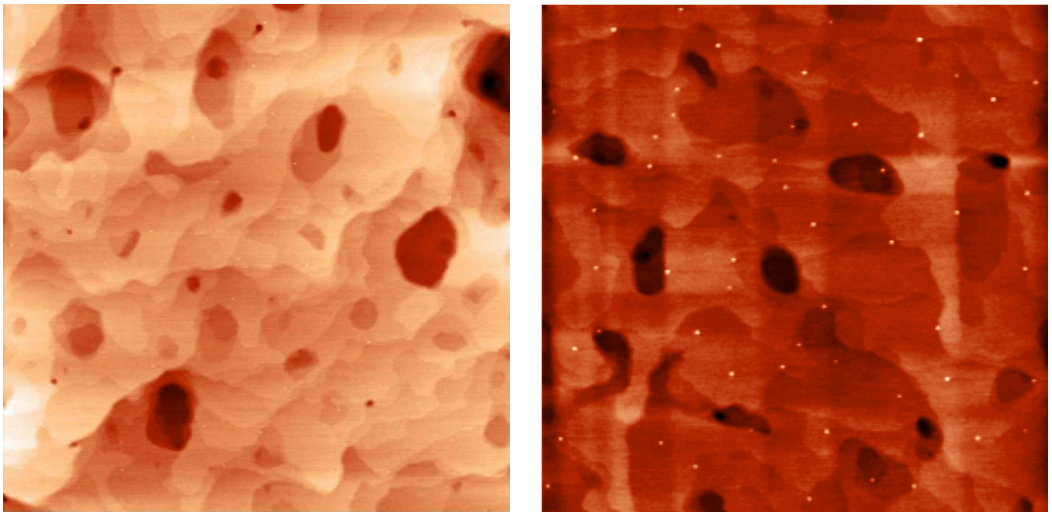

(a) (b)

Figure 6.1: Atomic force micrographs of (a) sample #0 (RMS roughness 1.0 nm, peak-to-peak 10 nm, scan area 5 μm×5 μm, height scale 10 nm), and (b) sample #2 (RMS roughness (0.47 nm, peak-to-peak 4.91 nm, scan area 3 μm×3 μm, height scale 6 nm). Figure (a) was acquired immediately after sample growth, whereas Figure (b) was obtained a year after sample growth. The small dots in Figure (b) were not seen in micrographs immediately after sample growth, so it is possible that the surface of the sample changes as a function of time.

10 nm, a rather high value for a nominally 20 nm thick layer. The determined RMS roughness was 1.0 nm. From the peak-to-peak height variation and the RMS roughness, it can be seen that the roughness is not normally distributed. There are many small >5nm deep holes. The quality of the surface was unsatisfactory for X-ray composition determination and the high surface roughness likely originates from the 70nm thick GaP buffer layer that was grown below the $GaAs_yP_{1-x-y}N_x$ layer. Similar evidence was observed from other samples possessing a GaP buffer layer. For this reason and because the XRD and XRR measurements have features not predicted by the theory, the step to grow the GaP buffer layer was omitted in

Table 6.2: Surface roughness of the samples as determined by AFM.

Sample	RMS roughness	peak-to-peak roughness
#0	1.0 nm	10 nm
#1	0.35 nm	2.54 nm
#2	0.47 nm	4.91 nm
#3	0.48 nm	4.43 nm
#4	0.62 nm	8.10 nm
#5	1.62 nm	9.90 nm

further samples[1].

The atomic force micrographs were taken from the samples #0–5 (some of these shown in Figure 6.1). The RMS roughness and the peak-to-peak roughness were determined with AFM based on a 3 μm $\times$ 3 μm scan area with the exception of sample #0 which had 5 μm $\times$ 5 μm scan area. The roughnesses determined by AFM are in Table 6.2. The AFM measurements were not performed for samples #6–9, and they were sent for RBS analysis so it is not possible to perform the AFM measurements afterwards for these samples.

The surface roughnesses of the samples are reasonably low with the exception of sample #5, which had a high surface roughness. The reason for this high surface roughness is unknown. Nevertheless, despite this high surface roughness of sample #5 the XRR and XRD measurements were chosen to be performed for all of these samples. It was later observed that despite the high surface roughness of sample #5, XRR was able to measure the electron density and layer thickness.

To obtain accurate reference values for layer compositions, the RBS and NRA measurements were performed for samples #1–9. The measurements were performed at Lawrence Berkeley National Laboratory by Kin Man Yu and the measurement results are listed in Table 6.3. The NRA measurements for the thin 30 nm thick samples were not performed because the N signals were too low to determine the

[1]It was later observed that the growth parameters of the GaP buffer layer were slightly off and afterwards atomically smooth GaP buffer layers were grown, but the samples in this thesis were grown with no GaP buffer layer.

Table 6.3: RBS and NRA results of the samples. f_{sub} refers to the substitutional fraction of N in the crystal lattice. x_{XRD} refers to the N content determined using XRD while keeping the RBS-determined As content as a fixed value.

Sample	Thickness	y_{RBS}	x_{NRA}	$\chi_{\mathrm{min,GaAsP}}$	$\chi_{\mathrm{min,N}}$	f_{sub}	x_{XRD}
#1	31 nm	0.31	?				0.007
#2	31.5 nm	0.34	?				0.006
#3	31 nm	0.32	?				0.004
#4	31 nm	0.22	?				0.004
#5	?	0	?				0.006
#6	≈120 nm	0	≈0.016	0.06	0.19	0.86	0.008
#7	124 nm	0.2	≈0.013	0.09	0.16	0.92	0.012
#8	125 nm	0.31	≈0.008				0.017
#9	120 nm	0.32	0.01				0.012

N content in these cases. The RBS measurements also give the thicknesses of the films, which were estimated by assuming an average atomic composition of the film from the measured As content and are accurate to about 5%. The RBS-determined thicknesses are probably more accurate than the XRD-determined thicknesses as the XRD spectra did not contain notable interference fringes and therefore the thickness with XRD is determined by the width of the diffraction peaks, which may be broadened due to factors such as low crystalline quality. For the 130 nm thick layers, NRA results were fitted by using the SIMNRA software [130] and using a thin InN thin film as a standard for N quantification. The accuracy of N content is about 10%. For a perfect crystal, the GaAsPN minimum yield ($\chi_{\mathrm{min,GaAsNP}}$), ratio of the channeling to the random yields, should be on the order of 0.04. However, for samples #6 and #7 the values of $\chi_{\mathrm{min,GaAsNP}}$ are significantly higher than that. This suggests that the defect density in these samples (particularly sample #7) is significantly higher giving rise to a higher dechanneling of the ion beam.

6.3 PR composition determination

In this section, PR and PL measurements results are presented and discussed. Additionally, the accuracy of PR measurements is verified by comparing them to the RBS/NRA results and to the location of the XRD peak. It is found that the PR measurements are accurate. However, PR composition determination could not be done at all for samples #4–5 because the features seen in the PR spectra were not clear enough.

6.3.1 PR and PL measurements

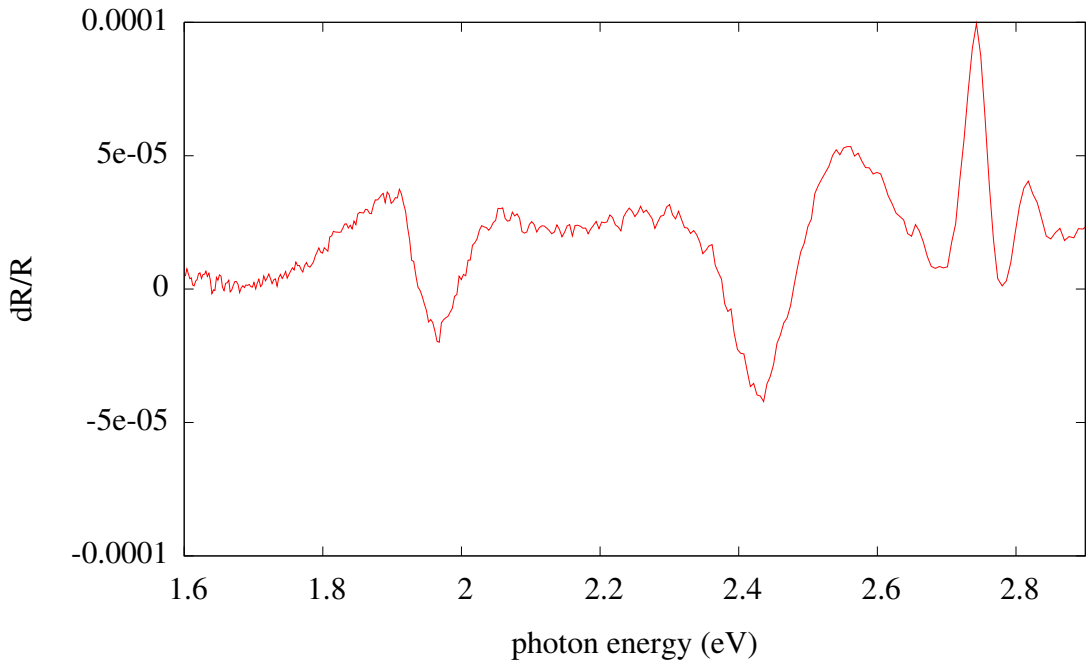

Figure 6.2: Measured PR spectrum from sample #0.

To study the accuracy of the developed PR based composition determination method, PR measurements were performed for samples #0–3. Figure 6.2 shows

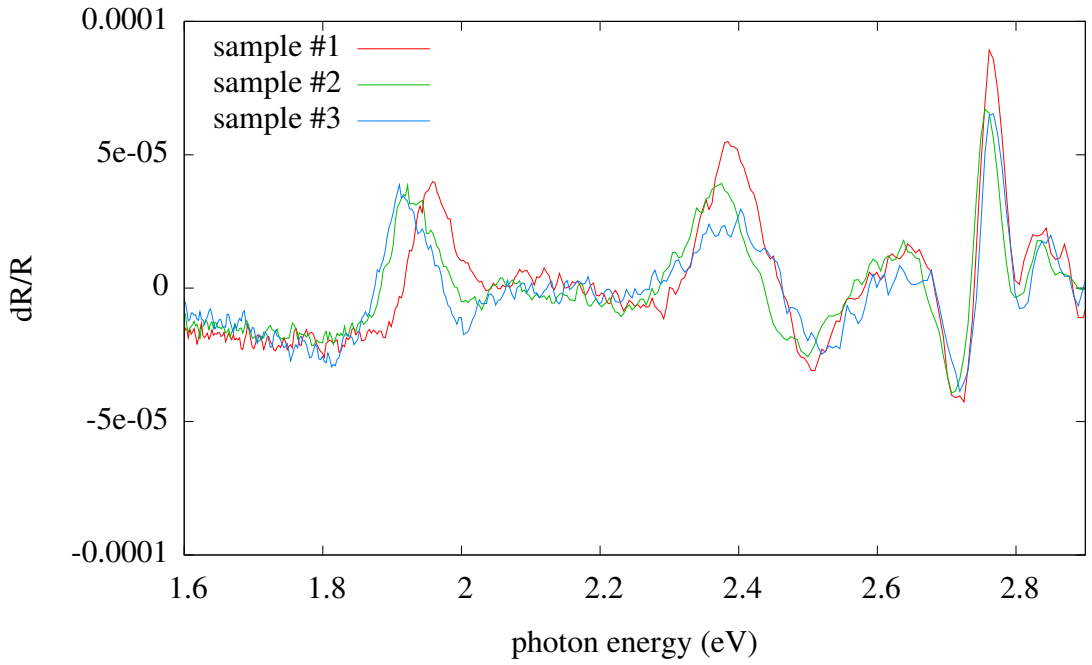

Figure 6.3: PR spectra for 30 nm thick GaAsPN samples #1–3. The reduction of band gap with an increasing arsenic content and the increasing separation between the transitions with an increasing nitrogen content can be clearly seen.

the PR spectrum measured from sample #0. The PR curve clearly shows that the conduction band is split into two: $E_+ = 2.48$ eV and $E_- = 1.93$ eV. It can be determined with the computer program in Appendix 2 that an arsenic content $y = 0.28$ and a nitrogen content $x = 0.005$ gives the values $E_+(0) = 2.48$ eV and $E_-(0) = 1.93$ eV.

The PR spectra from samples #1–3 having the same 30 nm layer thickness but varying arsenic and nitrogen compositions are shown in Figure 6.3. It can be clearly seen that the transitions in the PR spectrum move to a lower energy which corresponds to a lower band gap with increasing arsenic content, and that the distance between the transitions increases with increasing nitrogen content, as predicted by the BAC model.

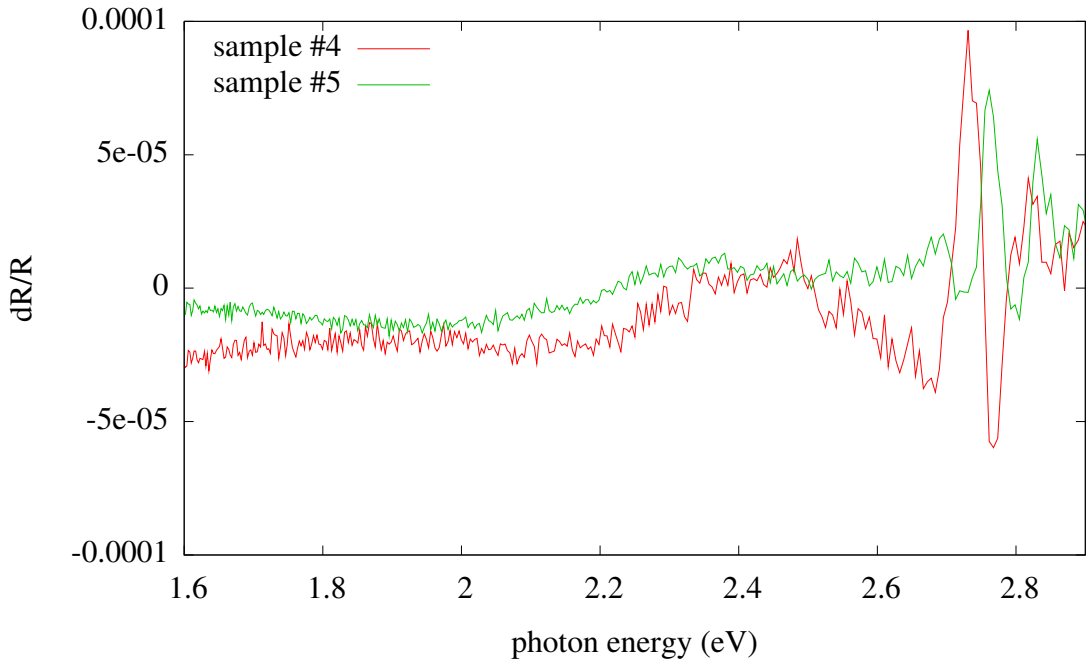

Figure 6.4: PR spectra for 30 nm thick GaAsPN samples #4–5. The substrate transition region is different for the two samples, suggesting that the substrate signal is overlapped with thin film signal. In addition to the substrate transition, another weak transition can be seen but its location is hard to define as the feature seen is rather wide. These PR spectra are unsuitable for composition determination.

The PR spectra from samples #4–5 are shown in Figure 6.4. In can be observed that the substrate transition region is different for the two samples, even though both used identical GaP wafers as the substrate. This is most straightforwardly explained by different phase in the lock-in amplifier. However, it is also possible that the substrate signal is overlapped with thin film E_+ signal for sample #4 having a low arsenic content. The E_+ transition is not seen at all for sample #5 due to the fact that the measurement apparatus is limited to 2.9 eV. Because of this, E_+ cannot be determined for these samples. Additionally, the features caused by E_- are rather wide and thus the location of E_- cannot in practice be determined from the spectra. Therefore, these PR spectra are unsuitable for composition determination.

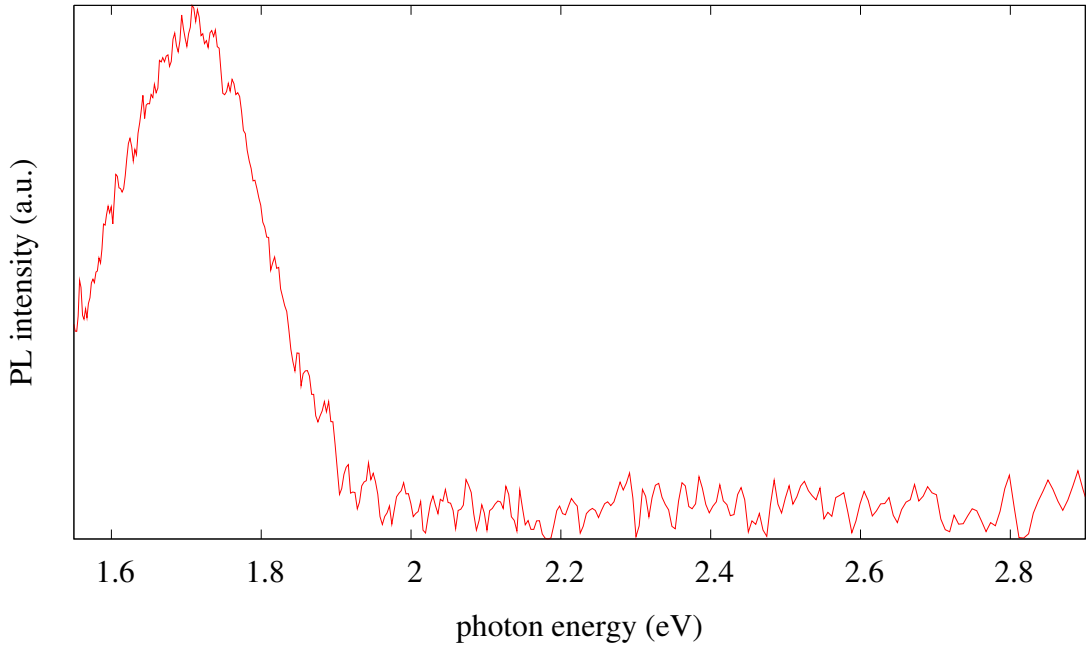

Figure 6.5: PL curve for sample #1. The curves for samples #2–3 (not shown) were practically identical in intensity and location of the peak. Samples #4–5 did not have PL and for samples #0 and #6–9 PL measurements were not performed.

The measurement apparatus is limited to 2.9 eV due to many reasons. Firstly, a 409 nm long-pass filter corresponding to a photon energy of 3.0 eV is used to block the 405 nm InGaN laser light. The transition between the passband and the stopband is obviously not completely sharp so it makes sense to limit the measurement range to less than 3.0 eV. Secondly, the overall sensitivity of the setup is weaker in this range because of the emission spectrum of the halogen lamp and the response of the detector.

The locations of the transitions were determined by fitting analysis from the PR spectra of samples #1–3 and are shown in Table 6.4. The PR measurements for the samples #6–9 were not performed, and the PR spectra from samples #4–5 are unsuitable for composition determination.

Table 6.4: Locations of the transitions in PR spectra and the compositions as determined by BAC model.

Sample	E_+ (eV)	E_- (eV)	y	x
#1	2.42 eV	1.94 eV	0.303	0.004
#2	2.41 eV	1.91 eV	0.324	0.005
#3	2.45 eV	1.89 eV	0.314	0.006

It should be noted that the GaAsPN samples #1–3 had red luminescence at room temperature. The PL spectrum was subtracted from the measured combined PL and PR spectrum with the same phase on the lock-in amplifier in order to obtain the PR spectrum. The PL spectrum of sample #1 is shown in Figure 6.5. The PL spectra of samples #2–3 are not shown, but are practically identical in intensity and in the location of the peak. Varying the nitrogen content or the arsenic content thus does not seem to affect the PL peak. A possible explanation for the PL peak is that it occurs via deep N-related states, as the peak does not seem to correspond to either of the band gaps. It has been shown that at least in GaPN the PL emission is dominated by optical transitions within deep states likely related to N clusters [131]. No PL was observed for samples #4–5. However, it should be noted that the PL was measured with PR measurement setup which has a lower sensitivity than a real PL setup due to the fact that lenses are not used in the same way to collect radiation across a wide range of angles. Therefore, it is possible that samples #4–5 had low luminescence not detectable by the measurement setup. The luminescence of samples #1–3 was even visible to the naked eye, and samples #4–5 had no luminescence visible to the naked eye. As the nitrogen contents of the samples were rather small, it is possible that the combined nitrogen and arsenic contents of samples #4–5 were not high enough to change the bandgap to a direct one, explaining the lack of bright PL. PL and PR spectra from samples #1–3 were measured immediately after sample growth and PL spectra from samples #4–5 were measured a year after sample growth. However, PL and PR spectra from sample #1 were additionally remeasured a year after sample growth and no changes in either

of the spectra were observed.

The fact that samples #4–5 did not have clearly visible features in the photoreflectance spectra and had no luminescence could be most straightforwardly explained by the layers having low crystalline quality. However, as later will be shown, XRD measurements indicate otherwise: according to XRD, layer #4 had practically as strong XRD peak as predicted by the theory unlike layers #1–3, indicating higher crystalline quality. It should be remembered that there are different types of crystalline defects (point defects, dislocations, stacking faults, etc). It is possible that the most common defect type in layer #4 is different from layers #1–3 thus causing no luminescence and weak photoreflectance features while at the same time not reducing the XRD peak intensity from the theoretically predicted one. One possible cause for the difference in PR spectra between samples #1–3 and #4–5 is the difference in As content. Another possible cause is that samples #1–3 were grown in the same day and #4–5 on another day. The MOVPE reactor had maintenance work done on it between the growth of samples #1–3 and #4–5, and the halogen lamp height needs to be adjusted during maintenance work. If the halogen lamp was at a lower height when samples #4–5 were grown when compared with the height when samples #1–3 were grown, the maximum temperature of the reactor was limited. The growth recipe during annealing uses the PID controller to set the target temperature of the thermocouple to be 750 °C but starts to count the annealing time when a lower temperature is reached. Thus, it is possible that samples #4–5 had lower effective annealing temperature than samples #1–3.

6.3.2 Agreement of PR compositions with XRD lattice constant

HRXRD measurements were made for sample #0. The diffraction peak from the thin film can be observed in the HRXRD measurement in addition to interference fringes that depend on the thickness of the thin film. It was assumed that the composition of N in the layer was 0.005 as determined by PR and BAC model calculations, and the composition of As was determined by fitting a simulated curve into the

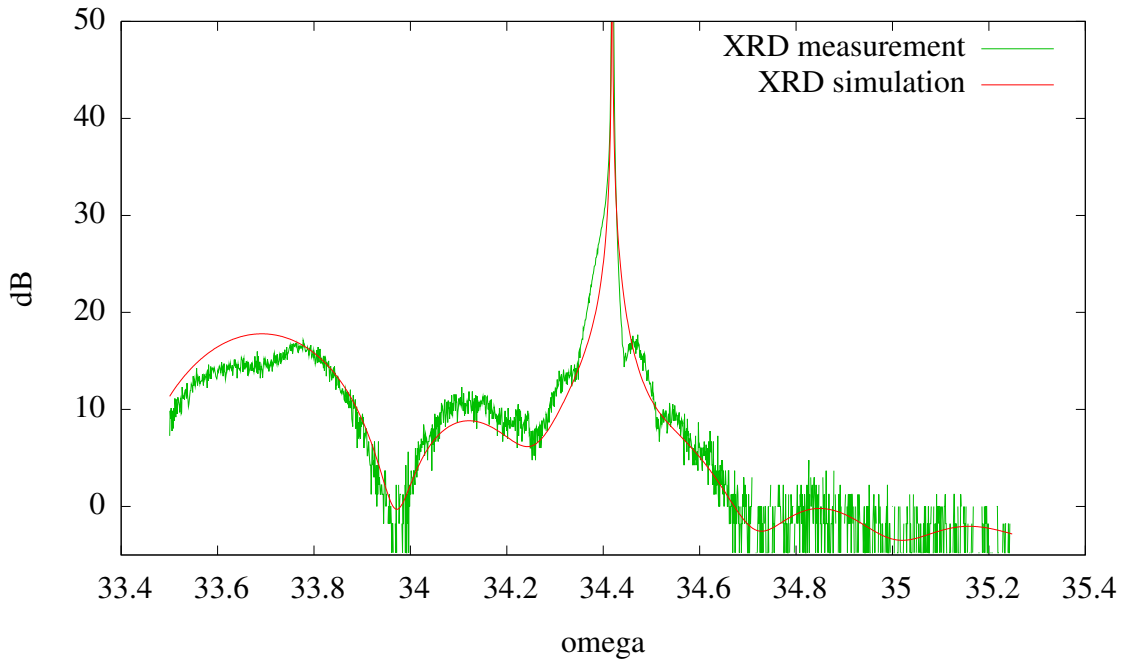

Figure 6.6: XRD curve of $GaAs_yP_{1-x-y}N_x$. The determined thickness was 17.9 nm and the composition $y = 0.30$ assuming $x = 0.005$.

measured HRXRD data. The composition was $y = 0.30$, but this is assuming that the composition of N is 0.005 which is a rough approximation calculated from the BAC model and may not necessarily be true. The result agrees with the $y = 0.28$ obtained from the BAC model calculations. In addition of being able to determine one free composition-related variable very accurately, fitting of a simulated curve into the measured HRXRD data also gives a layer thickness of 17.9 nm.

In the XRD curve of sample #0, it can be seen that the simulation does not reproduce the shape of the peaks exactly. This is an indication that the layer model consisting of one uniform and homogeneous layer is not necessarily good enough to accurately describe the sample. The difference between the simulation and the measurement likely originates from the slightly differing lattice constant and electric susceptibility between the MOVPE-grown GaP buffer layer and the doped substrate,

which can create interference effects.

Another way to calculate the composition of sample #0 would be to assume the value $y = 0.28$ as determined by the BAC model to be correct and calculate the nitrogen composition with fitting analysis from the XRD data. The value based on XRD fitting analysis is $x = 0.0026$ in that case. Of these values, $x = 0.005$ and $y = 0.30$ is probably more believable, as the used DMHy/V ratio was 0.32 and $GaP_{0.98}N_{0.02}$ has been previously grown with a DMHy/V ratio of 0.5 [132]. With XRD, it is possible to determine definitely that $y > 0.27$ for sample #0, as no amount of nitrogen can move the diffraction peak to the observed location for values of $y < 0.27$.

To determine whether PR-determined measurements agree with the lattice constant as determined by XRD, theoretical XRD curves were simulated with the PR-determined N contents. The intensity normalization factor, θ error offset, the layer thickness and the As content were fitted to the measured curves with the N content being fixed. Reasonably good agreement was obtained with the PR-determined results and the XRD-determined results, although the XRD-determined As contents seem to be systematically a bit larger than the values obtained from PR measurements. The results are in Table 6.5. For XRD measurements, the (004) reflection was used.

Table 6.5: Comparison of PR-determined As compositions with XRD-determined compositions based on lattice constant.

Sample	Fixed N content	PR As content	XRD As content
#0	0.005	0.277	0.298
#1	0.004	0.303	0.308
#2	0.005	0.324	0.337
#3	0.006	0.314	0.335

As a result of all the above, the good agreement between PR based composition determination method, XRD determined lattice constant and RBS/NRA results suggests that the PR based method gives accurate values for layer composition. It

is not entirely surprising that the PR based composition determination method is consistent with RBS/NRA results because the band-anticrossing model parameters have been most likely originally fitted using RBS/NRA data. However, it should be kept in mind that the BAC model is inaccurate and additionally that linear interpolation was used for the BAC model parameters, so the fact that such linear interpolation with the BAC model gives accurate composition values is certainly new information.

6.4 Relaxation and crystal plane tilt tests

It is possible that the crystal planes of an epitaxially grown thin film are tilted. For example, it has been found out that GaP layer grown on misoriented silicon surfaces relieves its strain energy by tilting the crystal planes [121]. Nevertheless, it should be kept in mind that crystal plane tilt is extremely improbable for a nominally exactly cut wafer like the wafers used. In order to determine whether the crystal planes of the grown GaAsPN layers are tilted, for samples #1–5 scans as a function of ω and the tilt angle Ψ were made of the thin film XRD peak of a symmetric reflection from planes parallel to the surface of the sample. The scans (not shown) indicate that the maximum of the peak occurs at the same values of $\omega - \theta$ offset angle and Ψ as the substrate peak. This indicates that the crystal planes are not tilted. Another way to check for crystal plane tilt would be to acquire reciprocal space maps (RSMs) of a symmetric reflection such as (002) or (004) and determining whether the thin film peak occurs at the same value of $\omega - \theta$ offset angle as the substrate peak. For perfectness, two such RSMs should be measured, one at a sample rotation angle of $\Phi = 0^\circ$ and another at a sample rotation angle of $\Phi = 90^\circ$. Some such RSMs were measured (not shown) and they are also fully consistent with no crystal plane tilt. The drawback of the RSM based method is their slow data acquisition time which typically easily exceeds an 8 h work day. Furthermore, the sample needs to be very carefully attached to the diffractometer, as with an adhesive tape based attachment method there is a drawback that the sample can creep. The probability of creep

increases as the data acquisition time is extended. Thus fast data acquisition time is here an advantage and therefore the method based on only rocking the sample along two directions in separate scans is more satisfactory.

Table 6.6: Relaxation tests: measured (004) reflection θ, calculated perpendicular lattice constant $a_\perp$, calculated $\omega - \theta$ offset difference α between substrate and fully strained thin film for (113) reflection, predicted θ for (113) reflection and actual measured θ for (113) reflection using the calculated offset difference.

Sample	(004) θ	$a_\perp$	α	predicted (113) θ	actual (113) θ
#1	33.645°	5.5612 Å	+0.449°	27.458°	27.459°
#2	33.573°	5.5716 Å	+0.491°	27.413°	27.415°
#3	33.599°	5.5679 Å	+0.476°	27.429°	27.432°
#4	33.896°	5.5248 Å	+0.301°	27.617°	27.624°
#5	34.518°	5.4373 Å	−0.054°	28.011°	28.012°

Table 6.7: Relaxation tests continued: calculated in-plane lattice constant $a_\parallel$, in-plane lattice constant difference between the thin film and the substrate and the calculated degree of relaxation R.

Sample	$a_\parallel$	$a_\parallel - a_s$	R
#1	5.4498 Å	-0.0007 Å	−0.012
#2	5.4496 Å	-0.0009 Å	−0.014
#3	5.4496 Å	-0.0009 Å	−0.015
#4	5.4493 Å	-0.0012 Å	−0.030
#5	5.4503 Å	-0.0002 Å	0.026

For samples #1–5, relaxation tests were performed. From Table 6.6, it can be seen that all of the samples are fully strained, because the measured location of the (113) peak is the very close to being the same as that predicted for a fully strained layer. Most importantly, the peak was actually observed at the predicted $\omega - \theta$ offset angle. Similarly, the calculated in-plane lattice constants and the degrees

of relaxation are shown in Table 6.7. It can be observed that the in-plane lattice constants are very close to the ones of the substrate. Due to the possible inaccuracy in the determined values (*e.g.* it is possible that the diffractometer goniometer is not completely accurate), most of the determined degrees of relaxation are slightly negative but close to 0. This means that in practice the degrees of relaxation can be considered to be 0.

The strain tests were not performed for the samples #6–9. Note, however, that it is likely that of the 130 nm thick samples #6–9 the samples #8–9 were partially relaxed. This is because assuming a similar discrepancy between the experimentally measured and theoretically calculated critical thickness as reported for $GaP_{0.98}N_{0.02}$ layers on GaP substrate [132], it can be estimated with calculations that the critical thickness of the GaAsPN layer in samples #6–9 are on the order of 175 nm, 140 nm, 60 nm and 60 nm, respectively. Unfortunately, the samples #6–9 were sent for RBS analysis and the samples are not in Finland, so it is not possible to do the relaxation tests afterwards for samples #6–9, some of which are likely relaxed. Additionally, some RSMs were measured and they are also fully consistent with no relaxation in the samples #1–5 and no strain gradient. The drawbacks of RSMs in comparison with the novel method are here the same as for checking crystal plane tilt.

Additionally, relaxation test was performed for the 220 nm thick sample previously analyzed in Ref. 132. The results show that the layer is fully strained. This is despite the fact that SR-XRT showed that the sample had few misfit dislocations. The results can be explained by the fact that SR-XRT and the XRD based relaxation check probe different things. SR-XRT probes the existence of misfit dislocations whereas XRD probes layer relaxation. Only few misfit dislocations will not noticeably change the in-plane lattice constant but will be visible in SR-XRT. This discrepancy between SR-XRT-determined critical thickness and XRD-determined critical thickness has been previously observed in Ref. 133 and Ref. 134.

Furthermore, relaxation test was performed for a GaAsP sample of unknown thickness. XRR measurements did not reveal notable interference fringes for the GaAsP sample. Thus, it is likely that the sample surface had high waviness or the sample was so thick that the resolution of the diffractometer was not enough

to observe the fine interference fringes. XRD measurements also did not reveal interference fringes from which the layer thickness could be determined, and the main XRD peak probably was broadened due to low crystal quality, so it is also not helpful in thickness determination. It has been previously observed that interference fringes in XRD measurements can disappear with increasing layer thickness [132]. The GaAsP layer had the thin film (004) peak at $\theta = 33.689^\circ$ corresponding to $a_\perp = 5.5548$ Å. The calculated value $\alpha = 0.421^\circ$ and the predicted $\theta_{113} = 27.486^\circ$. The observed θ_{113} was 27.458°, significantly smaller than the predicted location. The strained in-plane lattice constant was 5.4556 Å and the difference between it and the substrate lattice constant was 0.0051 Å, significantly larger than for the fully strained samples. The determined degree of relaxation R is 0.089. However, for this sample it should be remembered that the true peak in the 2-dimensional reciprocal space may not be paraxial so the determined degree of relaxation is only very approximate. As a matter of fact, the true peak was observed at $\theta = 27.475495^\circ$ with ω aligned so that it gives the maximum intensity. Using Bragg's law gives 1.66955 Å interplanal reflecting plane spacing. Taking into account the out-of-plane lattice constant 5.5548 Å results in an in-plane lattice constant of 5.4605 Å corresponding to a degree of relaxation of 0.167. This value determined with the true maximum of the peak and Bragg's law is probably more accurate than the inaccurate $a_\parallel$ determined from the parallel reciprocal lattice vector component using the peak that is not the true maximum of the peak. Thus, it can be concluded that for layers that are not fully strained, the relaxation test does not give accurate degree of relaxation values and can merely answer the question whether or not the layer is fully strained.

6.5 Full XRD (002) composition determination of GaAsPN

In this section, the composition of samples #1–9 is fully determined with the (002) XRD reflection. The obtained As contents mostly disagree with RBS+NRA deter-

mined values, being usually larger but for one sample the method was accurate. The accuracy of As content determination is found to be 0.12. Next, the failure of the experiments to reproduce the theoretical intensity is discussed, and a method to increase the accuracy of As content determination by taking into account the peak weakness is proposed. With the proposed method, the As content determination accuracy is 0.05.

6.5.1 Full XRD composition determination with no GaP buffer layer

To study the impact of the used fitting error function, the X-ray scan from the sample #1 was analyzed. Different trial As contents were tried for the four fitting error functions and the layer thickness, N content and the intensity normalization constant were fitted with the fixed As composition. Then the As content was assumed to be the one that results in the smallest possible fitting error function value. The plotted values of the different fitting error functions are in Figure 6.8. The determined As content, N content and layer thickness are in Table 6.8. From the table, it can be seen that the method is sensitive to the fitting error function used. Of the results, the value for F_4 (2-norm in logarithmic space) is the most believable, as it is closest to the values determined by RBS. This fitting error function also resulted in the best match between the measured curve and a simulation fitted to it, because it weighes equally all major features seen in the curve. Still, the determined N contents are rather large and the As contents are higher than those determined by RBS. It is likely that the peak intensity is reduced due to low crystalline quality, and the determined As content is too large, which results in the determined N content being too large so that the peak is still in the correct location.

To determine whether the measurement is repeatable, a second measurement was made for the sample #1 and it was analyzed by using two different fitting error functions F_2 (mixed relative/χ^2) and F_4 (2-norm in logarithmic space). By comparing Table 6.8 with Table 6.9, it can be estimated how much error the Poisson-distributed photon counting noise causes. The repeatability of the determined arsenic content

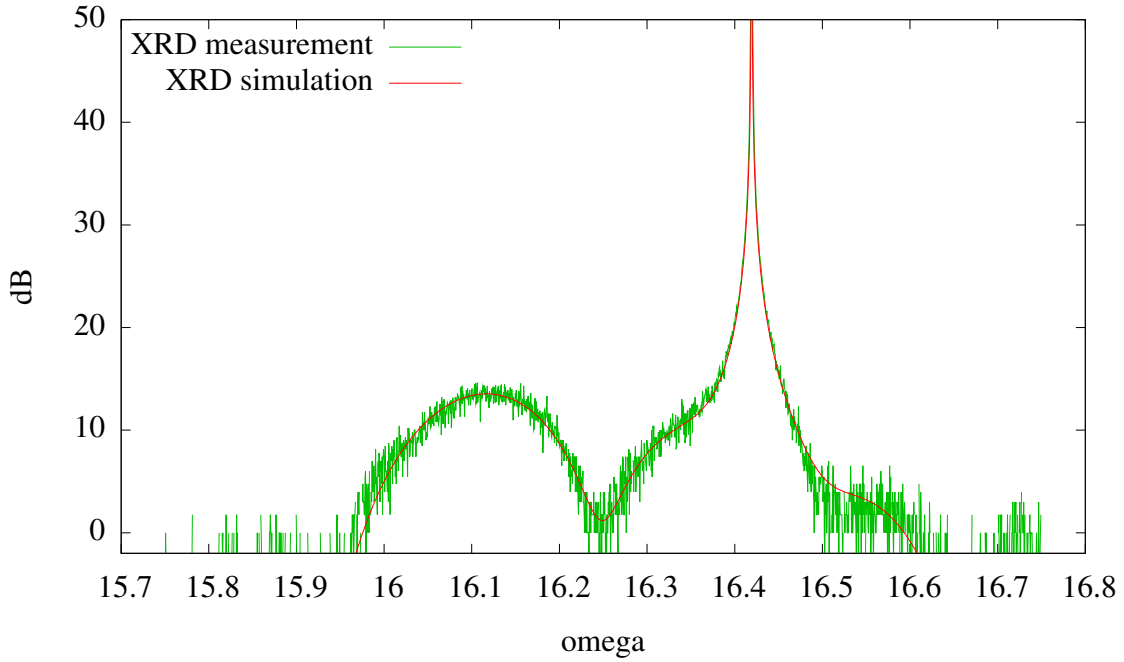

Figure 6.7: Measured XRD curve and a simulated curve that was fitted to the measured curve. An excellent fit was obtained.

Table 6.8: Determined As content, N content and thickness with different fitting error functions for sample #1.

Sample	Fitting error function	As content	N content	Layer thickness
#1	F_1	0.450	0.037	29.8 nm
#1	F_2	0.418	0.031	29.7 nm
#1	F_3	0.398	0.026	29.5 nm
#1	F_4	0.380	0.022	29.5 nm

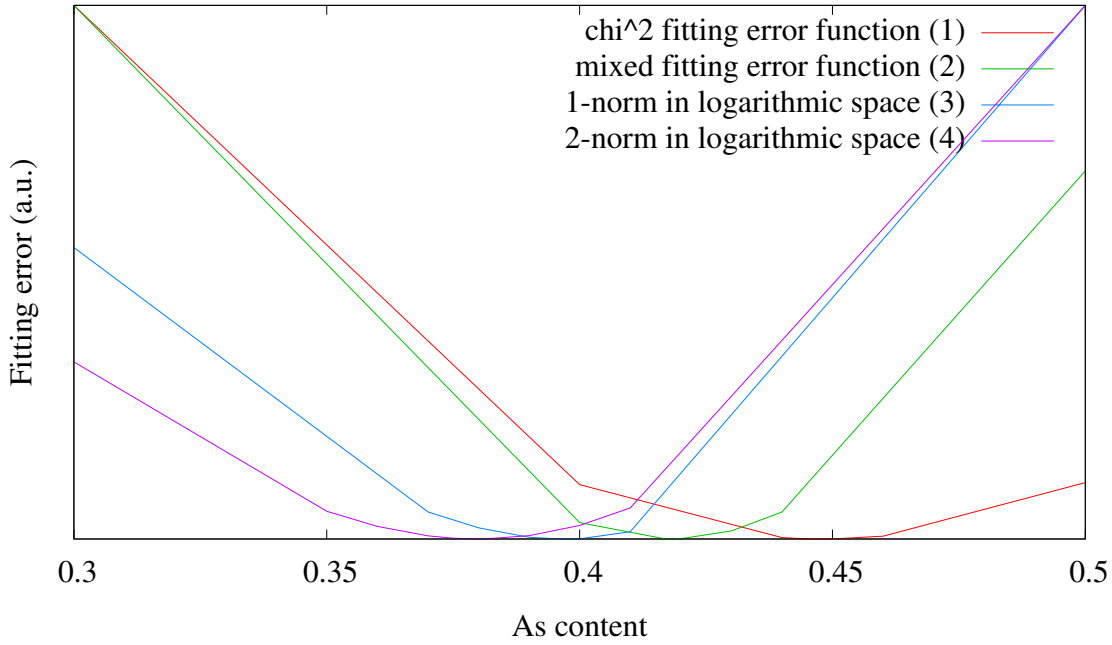

Figure 6.8: Minimum possible values of four different fitting error functions for different As contents for sample #1.

seems to be within an absolute error limit of 0.01. The fitting error function F_4 is chosen for the analysis of the rest of the samples, because it resulted in best visual agreement between the measured curve and the fitted curve, and additionally the determined As content agrees best with the RBS-determined values if the fitting error function F_4 is used.

The arsenic and nitrogen contents were determined for the samples #2–9. The arsenic precursor flow in sample #2 was increased compared to sample #1 with the nitrogen precursor flow being the same, and the nitrogen precursor flow in sample #3 was increased with the same arsenic precursor flow as in sample #2. The samples #4 and #5 were grown with a low and zero arsenic flow, respectively. The samples #6–9 are similar to samples #5, #4, #1 and #2, respectively, but are 130 nm thick. In this case, only one fitting error function was used, 2-norm in logarithmic space.

Table 6.9: Determined As content, N content and thickness with different fitting error functions for sample #1 with a second measurement to see if the results are repeatable.

Sample	Fitting error function	As content	N content	Layer thickness
#1	F_2	0.410	0.028	29.5 nm
#1	F_4	0.374	0.020	29.1 nm

Table 6.10: Determined As content, N content and thickness determined with logarithmic fitting error function for samples #2–9.

Sample	Fitting error function	As content	N content	Layer thickness
#2	F_4	0.456	0.031	27.7 nm
#3	F_4	0.439	0.030	28.2 nm
#4	F_4	0.219	0.004	29.6 nm
#5	F_4	0.082	0.025	29.6 nm
#6	F_4	0.229	0.058	132.5 nm
#7	F_4	0.693	0.119	99.7 nm
#8	F_4	0.787	0.120	62.3 nm
#9	F_4	0.776	0.110	64.7 nm

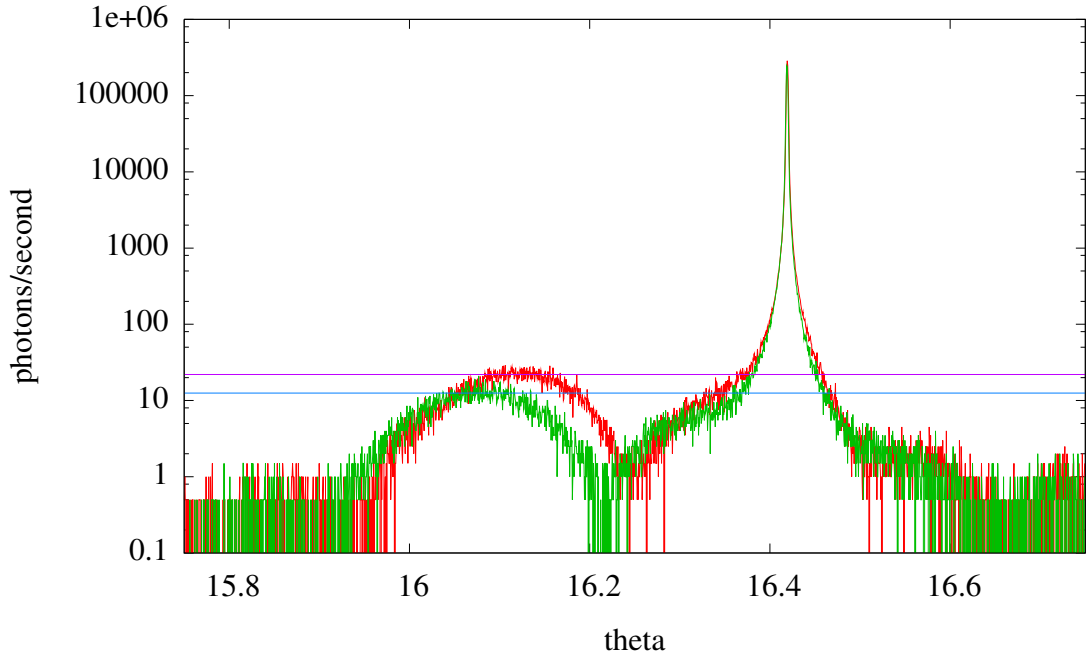

Figure 6.9: Two measured XRD curves with different arsenic contents and vertical lines denoting peak intensities.

The results are in Table 6.10.

The XRD peak for the sample #2 was at a slightly lower angle when compared with the peak of the sample #3, so at the same determined arsenic content the nitrogen content of sample #3 would be expected to be higher. However, the increase in the nitrogen content was not seen in the results as the determined arsenic content in sample #2 was higher than in sample #3. If we assume a priori that the arsenic content in sample #2 is 0.439, the fitting analysis gives a nitrogen content of 0.027. It is likely that the nitrogen content in sample #3 is higher than in sample #2, as the used dimethylhydrazine flow was higher. It seems that the arsenic content cannot be determined from the peak intensity accurately enough, and there is a crosserror between the arsenic content and the nitrogen content due to an accurately known peak location, which causes an error in the determined nitrogen content.

Finally, to show that the peak intensity varies in real measurements in addition to simulations, the measured XRD curves from the two first samples were plotted to Figure 6.9. It can be seen that even for this small change in arsenic content, the peak intensity changes noticeably, confirming the theory that was predicted by the simulations that the peak intensity varies as a function of changing layer arsenic content.

The potential error sources are listed in Section 5.2.2.2. However, not all error sources are applicable here. Because it has been determined that the layers are not fully strained, the error source related to layer relaxation cannot affect the measurement results. It has also been determined that the crystal planes are not tilted (see Section 6.4), so the error source related to that also cannot affect the measurement results. The measurement for sample #1 was performed twice, showing also that photon counting noise with the used averaging times is small enough for the method to be accurate with a repeatability in arsenic content being less than 0.01 absolute error. However, the used fitting error function seems to have effect on the location of the minimum of the fitting error function. Additionally, the error source related to low crystal quality is likely, as the XRD-determined As and N contents are higher than the RBS-determined As and N contents. In the next section, the weakness of the measured XRD peaks is discussed more.

6.5.2 Failure of the experiment to reproduce the theoretical intensity

Because the XRD-determined As and N contents are higher than the RBS-determined values, it seems that in the XRD measurements the peak intensities are weaker than predicted by theory. This seems to be the case for samples #1–3, #5 and especially for the 130 nm thick samples #6–9, but for the sample #4 XRD gives about the same As content as RBS (0.229 for XRD and 0.22 for RBS). Therefore, it seems likely that samples other than #4 have a reduced crystal quality. To investigate this more, the theoretical peak intensity was simulated for the (004) reflection of sample #2 so that the intensity normalization constant was fitted only

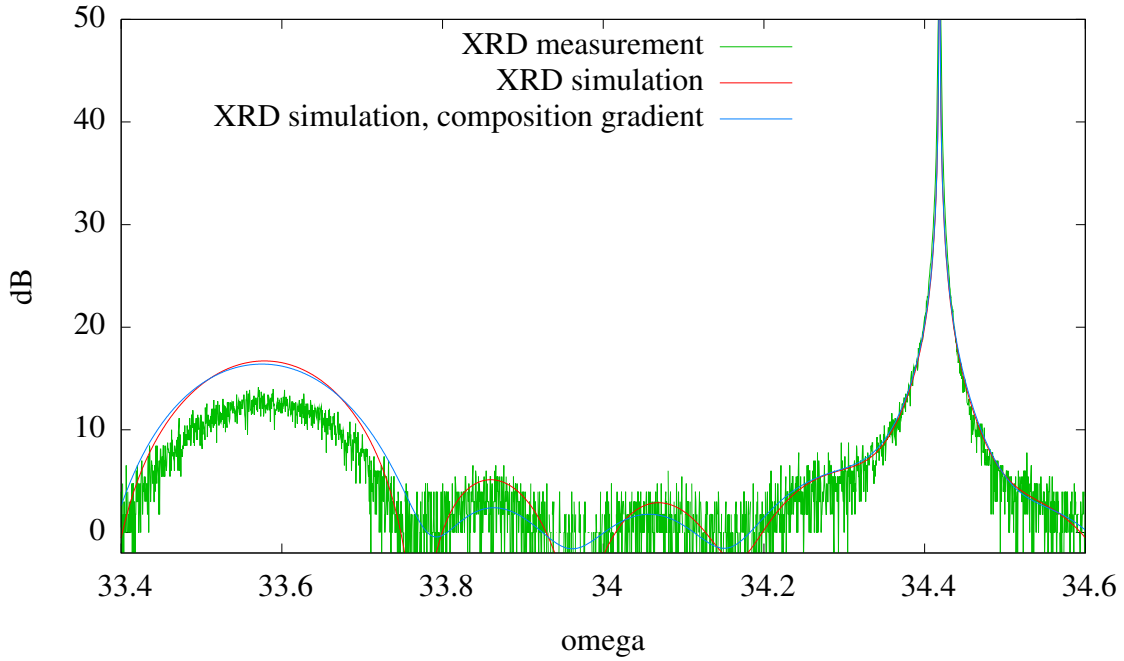

Figure 6.10: (004) reflection of sample #2 and a simulation fitted to it.

based on the substrate peak region. The fitted curve has a thin film peak stronger than in the measurement and different interference fringe modulation. The different interference fringe modulation suggests that the assumption of a homogeneous layer does not hold. It is possible that N is evaporated from the top of the layer during annealing, as annealing was performed with no DMHy flow. To investigate this more, a two-layer model was fitted into the measurement. The top layer had a different N content than the bottom layer. The resulting fit, shown in Figure 6.10, shows that the composition gradient of N does not explain the weakness of the thin film XRD peak but explains the interference fringe modulation. The weakness of the thin film XRD peak can be most straightforwardly explained by the presence of crystal defects.

As a conclusion for applying the method, the intensity of the (004) reflection should be checked. If the measured intensity is smaller than the theoretical intensity,

caution should be used when interpreting the results, as the (002) reflection will likely also be weaker than predicted by theory, causing the As content (and the N content) to be overestimated. In the next section, we will see if it's possible to take into account the weakness of the peaks in simulations.

Such crystal quality problems were not seen in a previous study where the composition of quaternary InAlAsSb was determined by using peak intensity in addition to peak location, but this may be due to the fact that MBE was used in the study, while here the layers were grown with MOVPE [120]. However, at the same time it should be remembered that the previous InAlAsSb study had only one data point, one material of zero Al content 'quaternary', *i.e.* InAsSb, for which the composition was determined by two independent methods. The accuracy of the method for the only other data point, a real InAlAsSb quaternary, was not validated with a method known to be accurate. Thus it could be argued that the study in this thesis is more rigorous than in the previous InAlAsSb study.

For example, it has been observed that carbon and hydrogen tends to be incorporated in MOVPE-grown layers of GaPN [135], GaN [136,137], GaInNAs [138,139], ZnO [140], GaAs [141, 142] and TiO_2 [143]. The incorporation of foreign atoms in the crystal structure obviously can affect the intensity of the reflection by reducing the crystal quality. It is also possible that nitrogen occupies interstitial sites in the crystal lattice due to the disparity in size of nitrogen and other group V atoms. These interstitial nitrogen atoms in the crystal lattice can cause strain fields around them. All of these effects can reduce the intensity of the reflection. As a matter of fact, the substitutional fraction determined by RBS/NRA measurements clearly suggested the presence of N intrestitials in the grown GaAsPN layers. It may be the case that our crystal quality problems are related to the special nature of GaAsPN, a dilute nitride. For example of an XRD curve from a material not containing nitrogen, see Figure 4.2 which contains an XRD curve of 53 nm thick layer of GaAsP on GaAs. It can be observed from Figure 4.2 that the measured layer peak is as strong as simulation predicts. This gives further support to our theory that nitrogen causes weak layer peaks. Additionally, it has been observed that MOVPE-grown layers of gallium phosphide on gallium phosphide have stacking faults [144]. So, in summary,

the weakness of the XRD peaks seen but that was not observed in the previous study can be due to (i) the special nature of dilute nitride alloys, (ii) due to the fact that MOVPE was used instead of MBE or (iii) due to stacking faults. It is interesting to note that the As content of sample #4 was reasonably accurately determined (0.229 by XRD and 0.22 by RBS), so it likely had a higher crystal quality. It is understandable that many of the grown materials have a low crystal quality, because the growth conditions of the materials were not optimized to achieve a good crystal quality. It can be hypothesized that an optimization of growth conditions could allow growing materials with the other compositions, too, with a good crystal quality.

6.5.3 Taking into account the weakness of the XRD peaks

To fully explain why the XRD peaks are weaker than predicted by theory in materials having low crystal quality, a better dynamical theory of XRD that is able to take into account crystallographic defects would be required. However, developing such a new theory of dynamical XRD is out of the scope of this thesis and the article published about this thesis [1]. However, it can be noted that within the traditional theory of dynamical XRD, the strength of the XRD peak is mainly determined by the susceptibility Fourier components $\chi_{\mathbf{h}}$ and $\chi_{\overline{\mathbf{h}}}$. As a matter of fact, the way changing the As content of GaAsPN changes the reflection intensity is actually by changing the values of these Fourier components. Multiplying these by a factor $w_{\mathbf{h}}$ between 0 and 1 makes the peak weaker. Note that the constant component χ_0 is not multiplied. This multiplication is not fully consistent with the dynamical theory of XRD, but is rather a simple trick to explain the weakness of the peak. The custom XRD curve fitting software was modified to support this multiplicative susceptibility factor to explain the weakness of the XRD peaks.

One difficulty with this method is that the $w_{(002)}$ required for accurate composition determination may differ from $w_{(004)}$, so a common w valid for both reflections cannot necessarily be determined from the (004) measurement for which knowing the composition is not necessary to determine $w_{(004)}$ as the reflection intensity and

thus the Fourier components of electric susceptibility are practically independent of material composition. However, for the (002) reflection for determining the correct value $w_{(002)}$ it is required to a priori know the composition unless $w_{(002)}$ could be somehow deduced from $w_{(004)}$. To see if there is a relationship between $w_{(002)}$ and $w_{(004)}$, the values for both were determined. The values were determined by assuming the RBS-determined As contents to be accurate. The values are shown in Table 6.11. It can be observed that for samples #1–6 $w_{(002)}$ is larger than $w_{(004)}$ but for samples #7–9 $w_{(004)}$ is larger than $w_{(002)}$. Thus there doesn't appear to be a general rule that could be used to determine $w_{(002)}$ from $w_{(004)}$. For all of the samples, the both the values of $w_{(002)}$ and the values of $w_{(004)}$ were always in the range from 0 to 1, indicating that the measured peaks are weaker than predicted by theory. They were never larger than 1. This is consistent with the fact that there is a factor that can reduce the intensity of an XRD peak (low crystal quality) but there is no known factor that can increase the intensity of an XRD peak.

Based on this limited set of samples, it seems to be the case that for thick layers having a large mismatch in lattice constants, $w_{(004)}$ is larger than $w_{(002)}$, whereas for layers having either small mismatch in lattice constants, a thin 30 nm thick film or both, $w_{(004)}$ is smaller than $w_{(002)}$. A transformation to calculate $w_{(002)}$ based on $w_{(004)}$ can be expressed as $w_{(002)} = f(w_{(004)})$ and would ideally have the properties $f(1) = 1$ for films of perfect crystal quality and $f(0) = 0$ for films that are fully amorphous. A set of functions that satisfies this relationship is $f(x) = x^{\alpha}$. The most important cases are the thin 30 nm thick films. Therefore α was determined from fitting analysis by using $w_{(002)}$ and $w_{(004)}$ determined for samples #1–6. The determined value of α is 0.392. It should be remembered, however, that this α value is probably valid only for a narrow range of growth conditions. The function $f(x) = x^{\alpha}$ is not useful for the 130 nm thick samples having a large mismatch between the lattice constants, at least with the fitted value of α. Figure 6.11 shows the values of $w_{(004)}$ and $w_{(002)}$ and the curve $f(x) = x^{0.392}$ fitted to the measurement results. Finally, Figure 6.12 demonstrates how the multiplicative susceptibility factor increases fit quality.

To see if the $w_{(002),\mathrm{calc}}$ is useful from composition determination point of view,

Table 6.11: $w_{(002)}$ and $w_{(004)}$ for the XRD measurements of the samples.

Sample	$w_{(002)}$	$w_{(004)}$	$w_{(002),\mathrm{calc}}$
#1	0.891	0.692	0.866
#2	0.788	0.594	0.815
#3	0.822	0.726	0.882
#4	0.984	0.911	0.964
#5	0.932	0.874	0.949
#6	0.710	0.373	0.679
#7	0.357	0.505	-
#8	0.264	0.383	-
#9	0.243	0.323	-

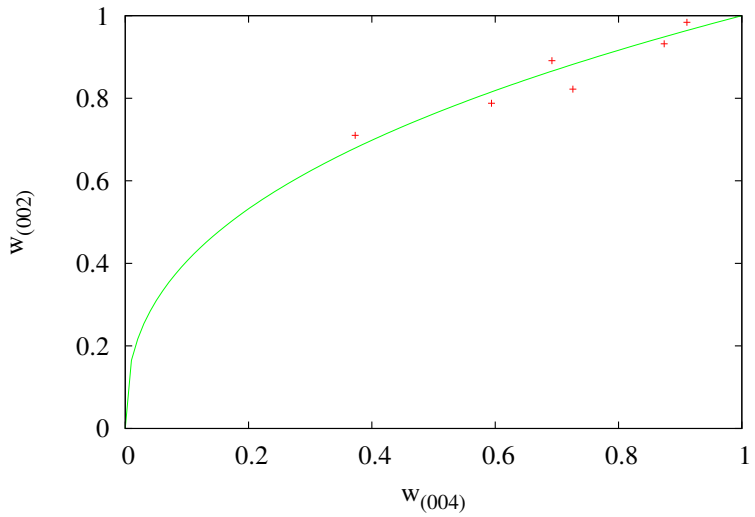

Figure 6.11: $w_{(004)}$ plotted against $w_{(002)}$ and the curve $w_{(002)} = {w_{(004)}}^{0.392}$ fitted to the data points.

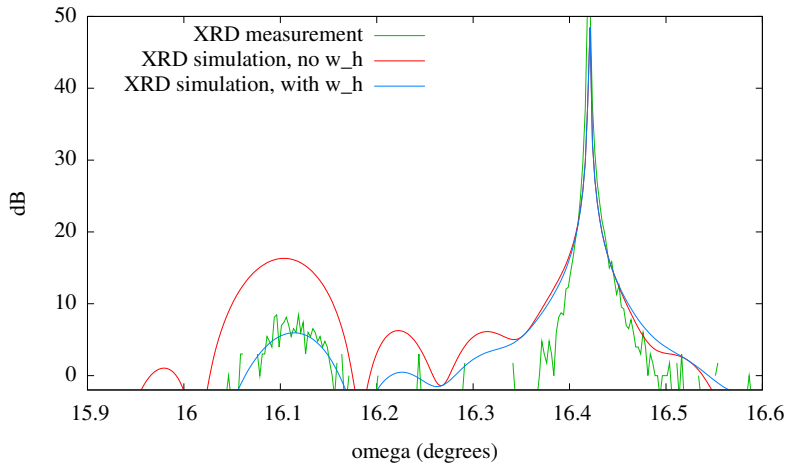

Figure 6.12: Measured XRD curve of the (002) reflection and a simulation fitted to it using the fixed RBS-determined As content. The simulation is fitted both with and without the multiplicative susceptibility factor $w_{(002)}$. The intensity normalization factor is fitted only using the substrate peak region.

Table 6.12: $w_{(002),\mathrm{calc}}$ and the As and N contents for the XRD measurements of the samples with peak weakness taken into account. Taking the peak weakness into account was found to be not suitable for samples #7–9, so only samples #1–6 are shown.

Sample	$w_{(002),\mathrm{calc}}$	y	x
#1	0.874	0.282	0.000
#2	0.826	0.360	0.010
#3	0.889	0.363	0.012
#4	0.905	0.205	0.004
#5	0.952	0.019	0.011
#6	0.696	0.000	0.008

for the samples #1–6 the As and N contents were determined by using the described quaternary composition determination method, this time with a value of $w \neq 1$. The previous results were determined with the default value of $w = 1$. The determined As and N contents are shown in Table 6.12. It can be seen that for sample #1, the determined nitrogen content is 0 which is unrealistic as there was a flow of DMHy when sample #1 was grown. The method of calculating $w_{(002),\mathrm{calc}}$ therefore is not fully satisfactory as it was unable to determine the inclusion of nitrogen in this layer. Nevertheless, the error in As content became smaller. With this method that takes into account the weakness of the XRD peak, the maximum error in the As content is about 0.05 and the maximum error in N content is about 0.01 in contrast to the maximum errors of 0.12 and 0.025 when the weakness of the XRD peak was not taken into account. For samples #7–9 having both high lattice constant mismatch and a thick film this method is not useful because the calculated $w_{(002),\mathrm{calc}}$ using $\alpha = 0.392$ markedly deviates from the real $w_{(002)}$.

6.6 Full XRR and XRD composition determination of GaAsPN

The full compositions of the layers were determined by the method described in Section 5.2.3. Multiple XRR measurements were performed per sample to investigate how accurate the XRR-determined electron density is. The fitting range of 0.25° to 1° was used to determine the XRR electron density. Note that 0.25° is just below the critical angle. The measurement results are shown in Table 6.13.

Note that the use of the custom mixed relative/χ^2 fitting error function is important. For example, the more commonly used 2-norm in logarithmic space fitting error function gives an incorrect electron density of $1.205{\cdot}10^{30}$ m^{-3} for sample #1 measurement 1, being 1% smaller than the correct electron density. Figure 6.13 illustrates how the theoretical electron density varies as a function of material As content. In the theoretical calculations, the N content corresponding to the trial As content is determined by fitting the XRD peak location.

Table 6.13: XRR and XRD composition determination of the layers. There were multiple XRR measurements per sample, but the XRD measurements were performed only once per sample. $a_\perp$ is the out-of-plane lattice constant determined from (004) XRD scans. ρ_e is the XRR-determined electron density. $y_{\mathrm{XRD+XRR}}$ and $x_{\mathrm{XRD+XRR}}$ are the As and N contents determined from both XRD and XRR scans. In comparison, the RBS-determined As contents for samples #1–5 are 0.31, 0.34, 0.32, 0.22 and 0. Sample #2 measurement 1 was misaligned leading to an incorrect determination of electron density and thus As and N contents.

Sample	Meas.	$a_\perp$	ρ_e	$y_{\mathrm{XRD+XRR}}$	$x_{\mathrm{XRD+XRR}}$
#1	1	5.56120 Å	$1.217 \cdot 10^{30}$ m^{-3}	0.316	0.006
#1	2		$1.219 \cdot 10^{30}$ m^{-3}	0.324	0.008
#1	3		$1.213 \cdot 10^{30}$ m^{-3}	0.305	0.004
#2	1	5.57124 Å	$1.241 \cdot 10^{30}$ m^{-3}	0.385	0.015
#2	2		$1.229 \cdot 10^{30}$ m^{-3}	0.353	0.008
#2	3		$1.223 \cdot 10^{30}$ m^{-3}	0.337	0.005
#3	1	5.56788 Å	$1.227 \cdot 10^{30}$ m^{-3}	0.348	0.009
#3	2		$1.224 \cdot 10^{30}$ m^{-3}	0.339	0.007
#3	3		$1.222 \cdot 10^{30}$ m^{-3}	0.331	0.006
#4	1	5.52372 Å	$1.180 \cdot 10^{30}$ m^{-3}	0.205	0.003
#4	2		$1.178 \cdot 10^{30}$ m^{-3}	0.199	0.002
#4	3		$1.193 \cdot 10^{30}$ m^{-3}	0.240	0.011
#5	1	5.44076 Å	$1.119 \cdot 10^{30}$ m^{-3}	0.016	0.009
#5	2		$1.112 \cdot 10^{30}$ m^{-3}	0.000	0.005
#5	3		$1.120 \cdot 10^{30}$ m^{-3}	0.020	0.010

It can be observed that for most samples, the XRR+XRD-determined As contents are close to the RBS-determined values having an error of at most 0.03, but for sample #2 one of the XRR+XRD-determined As contents has an error of more than 0.04. This is due to the fact that sample #2 measurement 1 was slightly misaligned: the full beam reflection for measurement 1 was 362 000 counts/s whereas it was 501 000 counts/s for measurement 2 and 464 000 counts/s for measurement 3. Thus measurements 2 and 3 give most accurate composition information for sample #2. The slightly misaligned sample was chosen to be included in this thesis, because it illustrates how a misaligned sample can lead to incorrectly determined composition.

The maximum difference between the RBS-determined As contents and the XRD+XRR-determined As contents is below 0.05 and the maximum difference between the RBS+XRD determined N contents and the newly determined N contents is below 0.01. Thus it can be concluded that the method is accurate to within 0.05 in As content and to within 0.01 in N content. However, if only perfectly aligned samples are considered, the maximum difference in As content between RBS and XRR+XRD is 0.03 and the maximum difference in N content is 0.007.

Sample #5 was a particularly interesting case. The measured XRR curve had no interference fringes visible to the human eye. Nevertheless, a computer with fitting analysis was able to determine the correct layer thickness and electron density. So, it can be concluded that the measurement indeed did contain interference fringes but they were so weak they were not visible to the human eye but were only visible to a computer. The XRR measurement of sample #5 is illustrated in Figure 6.14.

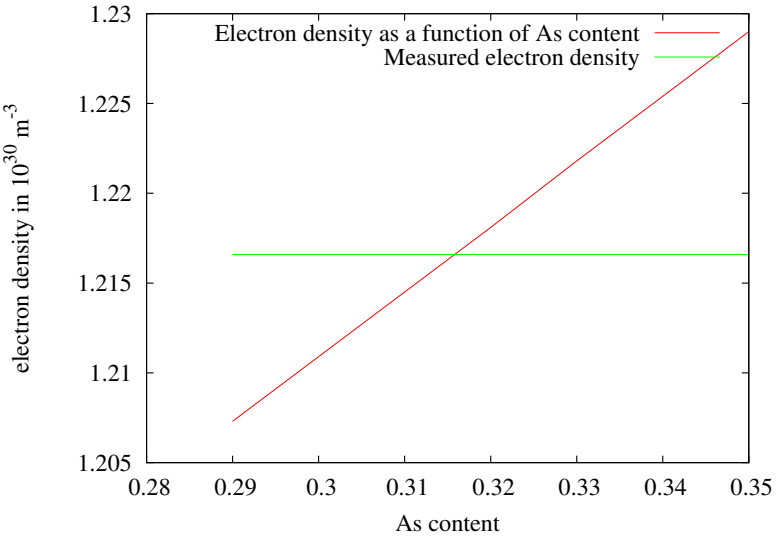

Figure 6.13: Simulated and measured electron density for sample #1 measurement 1. It can be observed that an electron density of 0.316 reproduces the measured value.

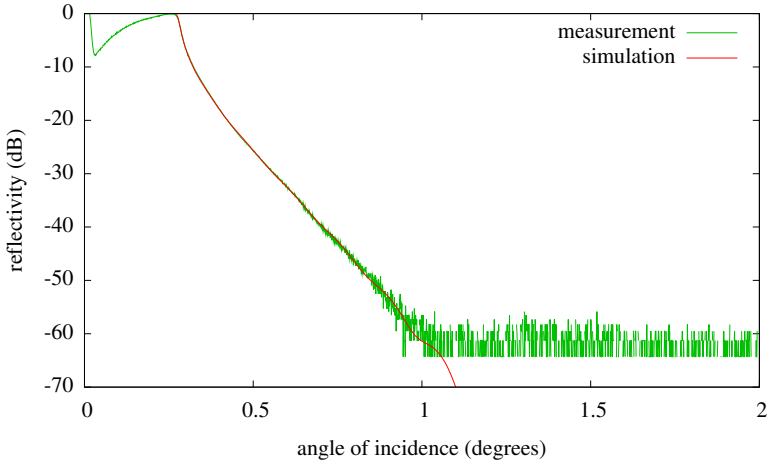

Figure 6.14: Simulated and measured XRR curves for sample #5.

7 Conclusions

Of all the binary III-V compound semiconductors, gallium phosphide has the lowest lattice constant mismatch when compared to silicon. Therefore gallium phosphide looks to be a promising material for a buffer layer grown on silicon on top of which optoelectronic components made from other III-V compound semiconductors can be integrated. The integration of optoelectronics with silicon CMOS microelectronics could allow building optical intra-chip and inter-chip interconnects.

XRR and XRD can be used to obtain information about the thickness of the thin film. The thickness measured with XRR and XRD agree well with each other. XRD can be used to measure the composition of a ternary compound semiconductor very accurately, but composition determination of a quaternary semiconductor is hard. A second composition-related variable in addition to the peak location is required. The intensity of the peak for an allowed reflection such as (004) varies only slightly as a function of the layer composition. However, for GaAsPN the intensity of a quasi-forbidden reflection such as (002) varies strongly as a function of the layer composition, and with a fitting analysis it is possible to obtain information about the composition of a quaternary material using a single X-ray measurement of a quasi-forbidden reflection. Additionally, the XRR-determined electron density can be used as a second composition dependent variable in addition to XRD peak location. When performing these measurements, the measured layer should be grown directly on top of gallium phosphide substrate. Growing a buffer layer of GaP between the substrate and the measured layer results in features in the measurements that cannot be reproduced by simulations. Furthermore, when performing XRR measurements

care should be taken to align the sample properly.

The BAC model predicts that the conduction band in dilute nitrides splits into two separate sub-bands. This allows the fabrication of an intermediate-band solar cell. PR can be used to observe the splitting of the conduction band into two. PR with BAC model calculations was found to be a suitable method to estimate the composition of a quaternary semiconductor. The results are in reasonably good agreement with the lattice constant as determined by XRD, but they do not agree with the XRD method where the intensity of the XRD peak was used in addition to the location of the peak. Furthermore, PR composition analysis worked only for samples #1–3 and not for samples #4–5.

To investigate more which of these methods is the most accurate, RBS and NRA measurements were performed. The RBS measurements indicate that the XRD measurements are accurate to within an error of 0.12 in As content and 0.025 in N content. This is a rather low accuracy. This low accuracy results from the measured XRD peaks being weaker than predicted by theory. The software was modified to take into account the weakness of XRD peaks by using a multiplicative susceptibility factor. For samples #1–6 for which the (004) reflection was measured and for which the multiplicative susceptibility factor obeys a relationship $w_{(002),\mathrm{calc}} = {w_{(004)}}^{0.392}$, the measurements were reanalyzed by using the calculated multiplicative susceptibility factor $w_{(002),\mathrm{calc}}$ in the simulations. This resulted in an accuracy of 0.05 in As content and 0.01 in N content. The accuracy now is better, but it should be noted that as the N contents in the samples were small, it is possible that the method determines an N content of zero, which is unrealistic as there was a DMHy flow during the growth conditions of all samples. This happened for sample #1.

The combined XRR and XRD measurements have an error of 0.05 in As content and 0.01 in N content, so the accuracy of using both XRR electron density and XRD peak location is the same as the improved XRD analysis. However, unlike the improved XRD analysis the mathematical basis of the combined XRR and XRD analysis is sound and therefore this method is more satisfying. However, care needs to be taken to align the sample properly as misalignment can result in an error in electron density and thus layer composition. If only perfectly aligned samples are

considered, the combined XRR and XRD analysis is better than the improved XRD analysis, having a maximum error of 0.03 in As content and 0.007 in N content.

The PR measurements seem to be more accurate than the XRD measurements, but it should be noted that PR composition determination was only successful for samples #1–3 which have a narrow range of As contents. For samples #4–5 with low and no As content, E_+ overlapped the substrate signal or was outside of the ranges of the measurement apparatus, and E_- was too wide to determine its location accurately. Thus, unlike the simplest version XRD analysis which at least works for all samples even though it is not accurate, the PR analysis does not work for some of the samples. Additionally, the combined XRR and XRD analysis is practically as accurate as PR analysis for samples #1–3 and works well for all samples unlike the PR analysis, so there is little reason to do PR composition determination if a diffractometer is available.

Future studies should investigate the XRD based quaternary composition determination method for other alloys than InAlAsSb and GaAsPN, and the XRR and XRD based quaternary composition determination method for other alloys than GaAsPN. Future studies should also use a wider range of As and N contents and a larger selection of layer thicknesses for the composition determination of GaAsPN. Also, future studies should use more multiple repeated XRD measurements of the same sample, which was done here for only one sample for XRD although repeated XRR measurements were made. Furthermore, in future studies the grown layers should be characterized in a more thorough manner using *e.g.* TEM [145, 146] and SR-XRT [147–149] to see if they contain stacking faults or dislocations. Additionally, a more accurate dynamical theory of XRD should be developed to take into account the presence of crystallographic defects. This theory should replace the proposed multiplicative susceptibility factor with no sound mathematical basis. The PR composition determination would also benefit from future work, *e.g.* testing it across a wider range of As and N contents, using more than one layer thickness and testing it also for other quaternary dilute nitrides than GaAsPN.

References

[1] J-.M Tilli, H. Jussila, K. M. Yu, T. Huhtio, and M. Sopanen. Composition determination of quaternary GaAsPN layers from single X-ray diffraction measurement of quasi-forbidden (002) reflection. *J. Appl. Phys.*, 115:203102, 2014.

[2] J.-M. Tilli. *Puolijohderakenteiden röntgendiffraktion sovitusanalyysi.* B.Sc. thesis, Helsinki University of Technology, Department of Electrical and Communications Engineering, Espoo, 2007.

[3] W. Shan, W. Walukiewicz, K. M. Yu, J. Wu, J. W. Ager III, E. E. Haller, H. P. Xin, and C. W. Tu. Nature of the fundamental band gap in GaN_xP_{1-x} alloys. *Appl. Phys. Lett.*, 76(22):3251–3253, 2000.

[4] W. Shan, W. Walukiewicz, J. W. Ager III, E. E. Haller, J. F. Geisz, D. J. Friedman, J. M. Olson, and S. R. Kurtz. Band anticrossing in GaInNAs alloys. *Phys. Rev. Lett.*, 82(6):1221–1224, 1999.

[5] W. Shan, K. M. Yu, W. Walukiewicz, J. Wu, J. W. Ager III, and E. E. Haller. Band anticrossing in dilute nitrides. *J. Phys.: Condens. Matter*, 16(31):S3355, 2004.

[6] J. Wu, W. Shan, and W. Walukiewicz. Band anticrossing in highly mismatched III–V semiconductor alloys. *Semicond. Sci. Technol.*, 17(8):860, 2002.

[7] W. Shan, W. Walukiewicz, K. M. Yu, J. W. Ager III, E. E. Haller, J. F. Geisz, D. J. Friedman, J. M. Olson, S. R. Kurtz, H. P. Xin, and C. W. Tu. Band anticrossing in III–N–V alloys. *Phys. Stat. Sol. B*, 223(1):75–85, 2001.

[8] J. Wu, W. Walukiewicz, K. M. Yu, J. W. Ager III, E. E. Haller, Y. G. Hong, H. P. Xin, and C. W. Tu. Band anticrossing in $GaP_{1-x}N_x$ alloys. *Phys. Rev. B*, 65(24):241303, 2002.

[9] I. A. Buyanova, M. Izadifard, A. Kasic, H. Arwin, W. M. Chen, H. P. Xin, Y. G. Hong, and C. W. Tu. Analysis of band anticrossing in GaN_xP_{1-x} alloys. *Phys. Rev. B*, 70(8):085209, 2004.

[10] A. Luque and A. Martí. Increasing the efficiency of ideal solar cells by photon induced transitions at intermediate levels. *Phys. Rev. Lett.*, 78(26):5014–5017, 1997.

[11] N. López, L. A. Reichertz, K. M. Yu, K. Campman, and W. Walukiewicz. Engineering the electronic band structure for multiband solar cells. *Phys. Rev. Lett.*, 106(2):28701, 2011.

[12] A. Marti and A. Luque. Intermediate band solar cells. *Adv. Sci. Technol.*, 74:143–150, 2011.

[13] A. Martí, E. Antolin, C. R. Stanley, C. D. Farmer, N. López, P. Diaz, E. Cánovas, P. G. Linares, and A. Luque. Production of photocurrent due to intermediate-to-conduction-band transitions: a demonstration of a key operating principle of the intermediate-band solar cell. *Phys. Rev. Lett.*, 97(24):247701, 2006.

[14] A. Martí, N. López, E. Antolin, E. Cánovas, C. Stanley, C. Farmer, L. Cuadra, and A. Luque. Novel semiconductor solar cell structures: The quantum dot intermediate band solar cell. *Thin Solid Films*, 511:638–644, 2006.

[15] A. Luque and A. Martí. The intermediate band solar cell: progress toward the realization of an attractive concept. *Adv. Mater.*, 22(2):160–174, 2010.

[16] A. Luque, A. Marti, N. Lopez, E. Antolin, E. Canovas, C. Stanley, C. Farmer, and P. Diaz. Operation of the intermediate band solar cell under nonideal space charge region conditions and half filling of the intermediate band. *J. Appl. Phys.*, 99(9):094503, 2006.

[17] Antonio Luque and Antonio Marti. A metallic intermediate band high efficiency solar cell. *Prog. Photovolt. Res. Appl.*, 9(2):73–86, 2001.

[18] S. Liebich, M. Zimprich, P. Ludewig, A. Beyer, K. Volz, W. Stolz, B. Kunert, N. Hossain, S. R. Jin, and S. J. Sweeney. MOVPE growth and characterization of Ga(NAsP) laser structures monolithically integrated on Si (001) substrates. In *Proc. ISLC*, pages 143–144, 2010.

[19] S. Liebich, M. Zimprich, A. Beyer, C. Lange, D. J. Franzbach, S. Chatterjee, N. Hossain, S. J. Sweeney, K. Volz, B. Kunert, and W. Stolz. Laser operation of Ga(NAsP) lattice-matched to (001) silicon substrate. *Appl. Phys. Lett.*, 99(7):071109, 2011.

[20] K. M. Yu, W. Walukiewicz, J. W. Ager, D. Bour, R. Farshchi, O. D. Dubon, S. X. Li, I. D. Sharp, and E. E. Haller. Multiband GaNAsP quaternary alloys. *Appl. Phys. Lett.*, 88(9):092110, 2006.

[21] S. Almosni, C. Robert, T. Nguyen Thanh, C. Cornet, A. Létoublon, T. Quinci, C. Levallois, M. Perrin, J. Kuyyalil, L. Pedesseau, A. Balocchi, P. Barate, J. Even, J. M. Jancu, N. Bertru, X. Marie, O. Durand, and A. Le Corre. Evaluation of InGaPN and GaAsPN materials lattice-matched to Si for multijunction solar cells. *J. Appl. Phys.*, 113(12):123509–123509, 2013.

[22] W. J. Bartels. Characterization of thin layers on perfect crystals with a multipurpose high resolution x-ray diffractometer. *J. Vac. Sci. & Technol. B*, 1(2):338–345, 1983.

[23] P. F. Fewster. X-ray diffraction from low-dimensional structures. *Semicond. Sci. Technol.*, 8(11):1915–1934, 1993.

[24] C. C. Chang. Auger electron spectroscopy. *Surf. Sci.*, 25(1):53–79, 1971.

[25] J. C. Riviere. Auger electron spectroscopy. *Contemp. Phys.*, 14(6):513–539, 1973.

[26] P. Williams. Secondary ion mass spectrometry. *Annu. Rev. Mater. Sci.*, 15(1):517–548, 1985.

[27] S. Rubin, T. O. Passell, and L. E. Bailey. Chemical analysis of surfaces by nuclear methods. *Anal. Chem.*, 29(5):736–743, 1957.

[28] C. Jeynes, R. P. Webb, and A. Lohstroh. Ion beam analysis: A century of exploiting the electronic and nuclear structure of the atom for materials characterisation. *Rev. Accel. Sci. Technol.*, 4(01):41–82, 2011.

[29] J. M. Hollander and W. L. Jolly. X-ray photoelectron spectroscopy. *Acc. Chem. Res.*, 3(6):193–200, 1970.

[30] R. Cesareo. *Ullmann's Encyclopedia of Industrial Chemistry*, chapter X-Ray Fluorescence Spectrometry. Wiley, 2010.

[31] L. Vegard. Die konstitution der mischkristalle und die raumfüllung der atome. *Z. Phys.*, 5(1):17–26, 1921.

[32] A. R. Denton and Ashcroft N. W. Vegard's law. *Phys. Rev. A*, 43(6):3161–3164, 1991.

[33] W. Shockley and H. J. Queisser. Detailed balance limit of efficiency of p-n junction solar cells. *J. Appl. Phys.*, 32(3):510–519, 1961.

[34] A. R. Laracuente and L. J. Whitman. Step structure and surface morphology of hydrogen-terminated silicon: (001) to (114). *Surf. Sci.*, 545(1–2):70–84, 2003.

[35] C. M. Johnson and Conibeer G. J. Limiting efficiency of generalized realistic c-Si solar cells coupled to ideal up-converters. *J. Appl. Phys.*, 112:103108, 2012.

[36] T. Katoda and M. Kishi. Heteroepitaxial growth of gallium phosphide on silicon. *J. Electron. Mater.*, 9(4):783–796, 1980.

[37] H Mori, M Ogasawara, M Yamamoto, and M Tachikawa. New hydride vapor phase epitaxy for GaP growth on Si. *Appl. Phys. Lett.*, 51(16):1245–1247, 1987.

[38] K. Volz, A. Beyer, W. Witte, J. Ohlmann, I. Nemeth, B. Kunert, and W. Stolz. GaP-nucleation on exact Si (001) substrates for III/V device integration. *J. Cryst. Growth*, 315(1):37–47, 2011.

[39] B. Kunert, I. Nemeth, S. Reinhard, K. Volz, and W. Stolz. Si (001) surface preparation for the antiphase domain free heteroepitaxial growth of GaP on Si substrate. *Thin Solid Films*, 517(1):140–143, 2008.

[40] H. Döscher, T. Hannappel, B. Kunert, A. Beyer, K. Volz, and W. Stolz. In situ verification of single-domain III-V on Si (100) growth via metal-organic vapor phase epitaxy. *Appl. Phys. Lett.*, 93(17):172110, 2008.

[41] TJ Grassman, MR Brenner, S Rajagopalan, R Unocic, R Dehoff, M Mills, H Fraser, and SA Ringel. Control and elimination of nucleation-related defects in GaP/Si (001) heteroepitaxy. *Appl. Phys. Lett.*, 94(23):232106, 2009.

[42] I. Németh, B. Kunert, W. Stolz, and K. Volz. Heteroepitaxy of GaP on Si: Correlation of morphology, anti-phase-domain structure and MOVPE growth conditions. *J. Cryst. Growth*, 310(7):1595–1601, 2008.

[43] H. Döscher, O. Supplie, S. Brückner, T. Hannappel, A. Beyer, J. Ohlmann, and K. Volz. Indirect in situ characterization of Si (100) substrates at the initial stage of III–V heteroepitaxy. *J. Cryst. Growth*, 315(1):16–21, 2011.

[44] H. Döscher and T. Hannappel. In situ reflection anisotropy spectroscopy analysis of heteroepitaxial GaP films grown on Si (100). *J. Appl. Phys.*, 107(12):123523, 2010.

[45] A. Beyer, J. Ohlmann, S. Liebich, H. Heim, G. Witte, W. Stolz, and K. Volz. GaP heteroepitaxy on Si (001): Correlation of Si-surface structure, GaP growth conditions, and Si-III/V interface structure. *J. Appl. Phys.*, 111(8):083534, 2012.

[46] H. Döscher, B. Kunert, A. Beyer, O. Supplie, K. Volz, W. Stolz, and T. Hannappel. In situ antiphase domain quantification applied on heteroepitaxial GaP growth on Si (100). *J. Vac. Sci. & Technol. B*, 28(4):C5H1–C5H6, 2010.

[47] I. Németh, B. Kunert, W. Stolz, and K. Volz. Ways to quantitatively detect antiphase disorder in GaP films grown on Si (001) by transmission electron microscopy. *J. Cryst. Growth*, 310(23):4763–4767, 2008.

[48] H. Jussila, S. Nagarajan, P. Mattila, J. Riikonen, T. Huhtio, M. Sopanen, and H. Lipsanen. Growth and characterization of GaP layers on silicon substrates by metal-organic vapour phase epitaxy. *Phys. Stat. Sol. C*, 9(7):1607–1609, 2012.

[49] B. Kunert, K. Volz, J. Koch, and W. Stolz. Direct-band-gap Ga(NAsP)-material system pseudomorphically grown on GaP substrate. *Appl. Phys. Lett.*, 88(18):182108, 2006.

[50] B. Kunert, K. Volz, I. Nemeth, and W. Stolz. Luminescence investigations of the GaP-based dilute nitride Ga(NAsP) material system. *J. Lumin.*, 121(2):361–364, 2006.

[51] B. Kunert, K. Volz, and W. Stolz. Dilute nitride Ga(NAsP)/GaP-heterostructures: toward a material development for novel optoelectronic functionality on Si-substrate. *Phys. Stat. Sol. B*, 244(8):2730–2739, 2007.

[52] B. Kunert, S. Zinnkann, K. Volz, and W. Stolz. Monolithic integration of Ga(NAsP)/(BGa)P multi-quantum well structures on (001) silicon substrate by MOVPE. *J. Cryst. Growth*, 310(23):4776–4779, 2008.

[53] S. Borck, S. Chatterjee, B. Kunert, K. Volz, W. Stolz, J. Heber, W. W. Ruhle, N. C. Gerhardt, and M. R. Hofmann. Lasing in optically pumped Ga(NAsP)/GaP heterostructures. *Appl. Phys. Lett.*, 89(3):031102–031102, 2006.

[54] B. Kunert, S. Reinhard, J. Koch, M. Lampalzer, K. Volz, and W. Stolz. First demonstration of electrical injection lasing in the novel dilute nitride Ga(NAsP)/GaP-material system. *Phys. Stat. Sol. C*, 3(3):614–618, 2006.

[55] B. Kunert, A. Klehr, S. Reinhard, K. Volz, and W. Stolz. Near room temperature electrical injection lasing for dilute nitride Ga(NAsP)/GaP quantum-well structures grown by metal organic vapour phase epitaxy. *Electron. Lett.*, 42(10):601–603, 2006.

[56] J. Chamings, A. R. Adams, S. J. Sweeney, B. Kunert, K. Volz, and W. Stolz. Temperature dependence and physical properties of Ga(NAsP)/GaP semiconductor lasers. *Appl. Phys. Lett.*, 93(10):101108, 2008.

[57] N. Hossain, S. J. Sweeney, S. Rogowsky, R. Ostendorf, J. Wagner, S. Liebich, M. Zimprich, K. Volz, B. Kunert, and W. Stolz. Reduced threshold current dilute nitride Ga(NAsP)/GaP quantum well lasers grown by MOVPE. *Electron. Lett.*, 47(16):931–933, 2011.

[58] H. Jussila, S. Nagarajan, T. Huhtio, H. Lipsanen, T. O. Tuomi, and M. Sopanen. Structural study of GaP layers on misoriented silicon (001) substrates by transverse scan analysis. *J. Appl. Phys.*, 111(4):043518, 2012.

[59] L. M. Miller and J. J. Coleman. Metalorganic chemical vapor deposition. *Crit. Rev. Solid State*, 15(1):1–26, 1988.

[60] G. B. Stringfellow. *Organometallic vapor-phase epitaxy: Theory and practice*. Academic Press, 1999.

[61] H. Jussila. *Fabrication of Indium Arsenide Quantum Dot Structure for Semiconductor Optical Amplifiers*. M.Sc. thesis, Aalto University, School of Science and Technology, Espoo, 2010.

[62] G. B. Stringfellow. *Organometallic vapor phase epitaxy: Theory and Practice*. ACAdemic Press, Inc., San Diego, 1989.

[63] B. Kunert, K. Volz, J. Koch, and W. Stolz. MOVPE growth conditions of the novel direct band gap, diluted nitride Ga(NAsP) material system pseudomorphically strained on GaP-substrate. *J. Cryst. Growth*, 298:121–125, 2007.

[64] G. Binnig, C. F. Quate, and C. Gerber. Atomic force microscope. *Phys. Rev. Lett.*, 56(9):930, 1986.

[65] D. Rugar and P. Hansma. Atomic force microscopy. *Phys. Today*, 43(10):23–30, 1990.

[66] E. Meyer. Atomic force microscopy. *Prog. Surf. Sci.*, 41(1):3–49, 1992.

[67] G. Meyer and N. M. Amer. Novel optical approach to atomic force microscopy. *Appl. Phys. Lett.*, 53(12):1045–1047, 1988.

[68] S. J. Hanley and D. G. Gray. *Atomic force microscopy*. CRC Press, Inc. Boca Raton, Fl, 1995.

[69] P. K. Hansma, V. B. Elings, O. Marti, and C. E. Bracker. Scanning tunneling microscopy and atomic force microscopy: application to biology and technology. *Science*, 242(4876):209–216, 1988.

[70] S. Morita, R. Wiesendanger, and E. Meyer. *Noncontact atomic force microscopy*, volume 1. Springer, 2002.

[71] F. J. Giessibl. Advances in atomic force microscopy. *Rev. Mod. Phys.*, 75(3):949, 2003.

[72] E. Chason and T. M. Mayer. Thin film and surface characterization by specular X-ray reflectivity. *Crit. Rev. Solid State*, 22(1):1–67, 1997.

[73] A. Van der Lee. Grazing incidence specular reflectivity: theory, experiment, and applications. *Solid State Sci.*, 2(2):257–278, 2000.

[74] K. N. Stoev and K. Sakurai. Review on grazing incidence x-ray spectrometry and reflectometry. *Spectrochim. Acta B*, 54(1):41–82, 1999.

[75] D. K. G. De Boer, A. J. G. Leenaers, and W. W. Van den Hoogenhof. Glancing-incidence x-ray analysis of thin-layered materials: A review. *X-Ray Spectrom.*, 24(3):91–102, 1995.

[76] J. Misiewicz, G. Sęk, R. Kudrawiec, and P. Sitarek. Photomodulated reflectance and transmittance: optical characterisation of novel semiconductor materials and device structures. *Thin Solid Films*, 450(1):14–22, 2004.

[77] J. Misiewicz, P. Sitarek, G. Sęk, and R. Kudrawiec. Semiconductor heterostructures and device structures investigated by photoreflectance spectroscopy. *Mater. Sci.*, 21(3):263–320, 2003.

[78] F. H. Pollak and H. Shen. Photoreflectance characterization of semiconductors and semiconductor heterostructures. *J. Electron. Mater.*, 19(5):399–406, 1990.

[79] H. Lipsanen. *Fotoreflektanssi.* Licentiate thesis, Helsinki University of Technology, Department of Computer Science, Espoo, 1990.

[80] R. J. Matyi, L. E. Depero, E. Bontempi, P. Colombi, A. Gibaud, M. Jergel, M. Krumrey, T. A. Lafford, A. Lamperti, M. Meduna, A. Van der Lee, and C. Wiemer. The international vamas project on x-ray reflectivity measurements for evaluation of thin films and multilayers-preliminary results from the second round-robin. *Thin Solid Films*, 516(22):7962–7966, 2008.

[81] P. Colombi, D. K. Agnihotri, V. E. Asadchikov, E. Bontempi, D. K. Bowen, C. H. Chang, L. E. Depero, M. Farnworth, T. Fujimoto, A. Gibaud, M. Jergel, M. Krumrey, T. A. Lafford, A. Lamperti, T. Ma, R. J. Matyi, M. Meduna, S. Milita, K. Sakurai, L. Shabel'nikov, A. Ulyanenkov, A. Van der Lee, and C. Wiemer. Reproducibility in x-ray reflectometry: results from the first world-wide round-robin experiment. *J. Appl. Cryst.*, 41(1):143–152, 2008.

[82] I. D. Feranchuk, A. A. Minkevich, and A. P. Ulyanenkov. About non-Gaussian behaviour of the Debye-Waller factor at large scattering vectors. *Eur. Phys. J. Appl. Phys.*, 24(01):21–26, 2003.

[83] J. Tiilikainen, V. Bosund, J.-M. Tilli, J. Sormunen, M. Mattila, T. Hakkarainen, and H. Lipsanen. Genetic algorithm using independent component analysis in x-ray reflectivity curve fitting of periodic layer structures. *J. Phys. D: Appl. Phys.*, 40(19):6000–6004, 2007.

[84] J. Tiilikainen, J.-M. Tilli, V. Bosund, M. Mattila, T. Hakkarainen, V.-M. Airaksinen, and H. Lipsanen. Nonlinear fitness-space-structure adaptation and principal component analysis in genetic algorithms: an application to x-ray reflectivity analysis. *J. Phys. D: Appl. Phys.*, 40(1):215–218, 2007.

[85] M. Bjorck and G. Andersson. GenX: an extensible X-ray reflectivity refinement program utilizing differential evolution. *J. Appl. Cryst.*, 40(6):1174–1178, 2007.

[86] A. Nelson. Co-refinement of multiple-contrast neutron/x-ray reflectivity data using MOTOFIT. *J. Appl. Cryst.*, 39(2):273–276, 2006.

[87] A. Ulyanenkov. LEPTOS: a universal software for x-ray reflectivity and diffraction. In *Proc. SPIE*, volume 5536, pages 1–15. International Society for Optics and Photonics, 2004.

[88] A. Ulyanenkov. Novel methods and universal software for hrxrd, xrr and gisaxs data interpretation. *Appl. Surf. Sci.*, 253(1):106–111, 2006.

[89] L. G. Parratt. Surface studies of solids by total reflection of x-rays. *Phys. Rev.*, 95(2):359–369, Jul 1954.

[90] L. Névot and P. Croce. Caractérisation des surfaces par réflexion rasante de rayons x. application à l'étude du polissage de quelques verres silicates. *Rev. Phys. Appl.*, 15(3):761–779, 1980.

[91] X.-C. Liu, M. Myronov, A. Dobbie, V. H. Nguyen, and D. R. Leadley. Accuracy of thickness measurement for Ge epilayers grown on SiGe/Ge/Si (100) heterostructure by x-ray diffraction and reflectivity. *J. Vac. Sci. Technol. B*, 29(1):011010, 2011.

[92] O. M. Lugovskaya and S. A. Stepanov. Calculation of the polarizabilities of crystals for diffraction of x-rays of the continuous spectrum at wavelengths of 0.1-10 Å. *Sov. Phys.—Crystallogr.*, 36(4):478–481, 1991.

[93] D. Waasmaier and A. Kirfel. New analytical scattering-factor functions for free atoms and ions. *Acta Cryst.*, A51(3):416–431, 1995.

[94] B. L. Henke, E. M. Gullikson, and J. C. Davis. X-ray interactions: photoabsorption, scattering, transmission, and reflection at E=50-30000 eV, Z=1-92. *Atom. Data Nucl. Data*, 54(2):181–342, 1993.

[95] L.-M. Peng, G. Ren, S. L. Dudarev, and M. J. Whelan. Debye-Waller factors and absorptive scattering factors of elemental crystals. *Acta Cryst.*, A52(3):456–470, 1996.

[96] W. J. Bartels, J. Hornstra, and D. J. W. Lobeek. X-ray diffraction of multilayers and superlattices. *Acta Cryst.*, A42(6):539–545, 1986.

[97] R. Storn and K. Price. Differential evolution — a simple and efficient adaptive scheme for global optimization over continuous spaces. Technical Report TR-95-012, International Computer Science Institute, 1995.

[98] K. V. Price. Differential evolution: a fast and simple numerical optimizer. In *Proc. NAFIPS'96*, pages 524–527, 1996.

[99] R. Storn and K. Price. Differential evolution–a simple and efficient heuristic for global optimization over continuous spaces. *J. Global Optim.*, 11(4):341–359, 1997.

[100] K. V. Price, R. M. Storn, and J. A. Lampinen. *Differential Evolution: A Practical Approach to Global Optimization*. Springer-Verlag, 2005.

[101] M. Wormington, C. Panaccione, K. M. Matney, and D. K. Bowen. Characterization of structures from X-ray scattering data using genetic algorithms. *Phil. Trans. R. Soc. A*, 357(1761):2827–2848, 1999.

[102] M. Bjorck. Fitting with differential evolution: an introduction and evaluation. *J. Appl. Cryst.*, 44(6):1198–1204, 2011.

[103] A. D. Dane, A. Veldhuis, D. K. G. de Boer, A. J. G. Leenaers, and L. M. C. Buydens. Application of genetic algorithms for characterization of thin layered materials by glancing incidence X-ray reflectometry. *Phys. B*, 253(3–4):254–268, 1998.

[104] A. Ulyanenkov, K. Omote, and J. Harada. The genetic algorithm: refinement of X-ray reflectivity data from multilayers and thin films. *Phys. B*, 283(1–3):237–241, 2000.

[105] A. Ulyanenkov and S. Sobolewski. Extended genetic algorithm: application to x-ray analysis. *J. Phys. D: Appl. Phys.*, 38(10A):A235–A238, 2005.

[106] K. Levenberg. A method for the solution of certain problems in least squares. *Quart. Appl. Math.*, 2:164–168, 1944.

[107] D. W. Marquardt. An algorithm for least-squares estimation of nonlinear parameters. *J. Soc. Ind. Appl. Math.*, 11(2):431–441, 1963.

[108] J. A. Nelder and R. Mead. A simplex method for function minimization. *Comput. J.*, 7(4):308–313, 1965.

[109] S. Kirkpatrick, C. D. Gelatt, and M. P. Vecchi. Optimization by simulated annealing. *Science*, 220(4598):671–680, 1983.

[110] V. Černỳ. Thermodynamical approach to the traveling salesman problem: An efficient simulation algorithm. *J. Optimiz. Theory App.*, 45(1):41–51, 1985.

[111] S. A. Stepanov. X-ray server: an online resource for simulations of x-ray diffraction and scattering. In *Proc. SPIE*, volume 5536, pages 16–26, 2004.

[112] S. A. Stepanov, E. A. Kondrashkina, R. Koehler, D. V. Novikov, G. Materlik, and S. M. Durbin. Dynamical x-ray diffraction of multilayers and superlattices: Recursion matrix extension to grazing angles. *Phys. Rev. B*, 57(8):4829–4841, 1998.

[113] O. Reentilä, A. Lankinen, M. Mattila, A. Säynätjoki, T. O. Tuomi, and H. Lipsanen. In-situ optical reflectance and synchrotron X-ray topography study of defects in epitaxial dilute GaAsN on GaAs. *J. Mater. Sci. Mater. Electron.*, 19(2):137–142, 2008.

[114] J. Lemettinen. *Fotoreflektanssimittalaitteisto galliumfosfidinäytteille*. B.Sc. thesis, Aalto University, School of Electrical Engineering, Espoo, 2013.

[115] G. Bentoumi, V. Timoshevskii, N. Madini, M. Côté, R. Leonelli, J.-N. Beaudry, P. Desjardins, and R. A. Masut. Evidence for large configuration-induced band-gap fluctuations in $GaAs_{1-x}N_x$ alloys. *Phys. Rev. B*, 70(3):035315, 2004.

[116] X. Sun and J. M. Rorison. Modelling of the effects of conduction band fluctuations caused by nitrogen clustering in gainnas materials. *Phys. Stat. Sol. C*, 8(5):1646–1649, 2011.

[117] J. Tiilikainen, J.-M. Tilli, V. Bosund, M. Mattila, T. Hakkarainen, J. Sormunen, and H. Lipsanen. Accuracy in x-ray reflectivity analysis. *J. Phys. D: Appl. Phys.*, 40(23):7497–7501, 2007.

[118] J. Tiilikainen, M. Mattila, T. Hakkarainen, and H. Lipsanen. Novel method for error limit determination in x-ray reflectivity analysis. *J. Phys. D: Appl. Phys.*, 41(11):115302, 2008.

[119] H. Sonomura, T. Nanmori, S. Saito, and T. Miyauchi. Composition determination of $Al_xGa_{1-x}P$ alloys using diffracted x-ray intensities. *J. Appl. Phys.*, 45(11):5109–5111, 1974.

[120] D. J. Wallis, A. M. Keir, M. T. Emeny, and T. Martin. Measurement of III-V quaternary composition using X-ray diffraction. *IEE Proc. - Optoelectron.*, 148(2):97–100, 2001.

[121] Y. Takagi, Y. Furukawa, A. Wakahara, and H. Kan. Lattice relaxation process and crystallographic tilt in GaP layers grown on misoriented Si(001) substrates by metalorganic vapor phase epitaxy. *J. Appl. Phys.*, 107(6):063506, 2010.

[122] A. Krier, M. de la Mare, P. J. Carrington, M. Thompson, Q. Zhuang, A. Patanè, and R. Kudrawiec. Development of dilute nitride materials for mid-infrared diode lasers. *Semicond. Sci. Technol.*, 27(9):094009, 2012.

[123] H. Jussila, K. M. Yu, J. Kujala, F. Tuomisto, S. Nagarajan, J. Lemettinen, T. Huhtio, T. O. Tuomi, H. Lipsanen, and M. Sopanen. Substitutionality of nitrogen atoms and formation of nitrogen complexes and point defects in GaPN alloys. *J. Phys. D: Appl. Phys.*, 47:075106, 2014.

[124] Y.-K. Kuo, B.-T. Liou, S.-H. Yen, and H.-Y. Chu. Vegard's law deviation in lattice constant and band gap bowing parameter of zincblende $In_xGa_{1-x}N$. *Opt. Commun.*, 237(4):363–369, 2004.

[125] R. E. Nahory, M. A. Pollack, W. D. Johnston Jr, and R. L. Barns. Band gap versus composition and demonstration of Vegard's law for $In_{1-x}Ga_xAs_yP_{1-y}$ lattice matched to InP. *Appl. Phys. Lett.*, 33(7):659–661, 1978.

[126] P. Bergese, E. Bontempi, and L. E. Depero. A simple solution to systematic errors in density determination by X-ray reflectivity: The XRR-density evaluation (XRR-DE) method. *Appl. Surf. Sci.*, 253(1):28–32, 2006.

[127] Y. Fujii. Improvement of X-ray reflectivity calculations on a multilayered surface. *Powder Diffr.*, 28(2):100–104, 2013.

[128] S. Pereira, M. R. Correia, E. Pereira, K. P. O'Donnell, E. Alves, A. D. Sequeira, N. Franco, I. M. Watson, and C. J. Deatcher. Strain and composition distributions in wurtzite InGaN/GaN layers extracted from x-ray reciprocal space mapping. *Appl. Phys. Lett.*, 80(21):3913–3915, 2002.

[129] S. Sintonen. *Superhilarakenteiden karakterisointi röntgendiffraktio- ja röntgenheijastusmenetelmillä.* M.Sc. thesis, Helsinki University of Technology, Department of Electrical and Communications Engineering, Espoo, 2009.

[130] M. Mayer. SIMNRA, a simulation program for the analysis of NRA, RBS and ERDA. In *AIP Conf. Proc.*, volume 475, page 541, 1999.

[131] I. A. Buyanova, G. Y. Rudko, W. M. Chen, H. P. Xin, and C. W. Tu. Radiative recombination mechanism in GaN_xP_{1-x} alloys. *Appl. Phys. Lett.*, 80(10):1740–1742, 2002.

[132] H. Jussila, S. Nagarajan, S. Sintonen, S. Suihkonen, A. Lankinen, T. Huhtio, C. Paulmann, H. Lipsanen, T.O. Tuomi, and M. Sopanen. Evaluation of critical thickness of $GaP_{0.98}N_{0.02}$ layer on GaP substrate by synchrotron X-ray diffraction topography. *Thin Solid Films*, 534:680–684, 2013.

[133] J. Toivonen. *Growth and properties of GaAsN structures.* PhD thesis, Helsinki University of Technology, Department of Electrical and Communications Engineering, Espoo, 2003.

[134] A. Lankinen. *Synchrotron X-Ray Diffraction Topography of Semiconductor Heterostructures*. PhD thesis, Aalto University, School of Electrical Engineering, Espoo, 2012.

[135] J. F. Geisz, R. C. Reedy, B. M. Keyes, and W. K. Metzger. Unintentional carbon and hydrogen incorporation in GaNP grown by metal-organic chemical vapor deposition. *J. Cryst. Growth*, 259(3):223–231, 2003.

[136] G.-C. Yi and B. W. Wessels. Carbon–hydrogen complexes in vapor phase epitaxial GaN. *Appl. Phys. Lett.*, 70(3):357–359, 1997.

[137] D. D. Koleske, A. E. Wickenden, R. L. Henry, and M. E. Twigg. Influence of MOVPE growth conditions on carbon and silicon concentrations in GaN. *J. Cryst. Growth*, 242(1):55–69, 2002.

[138] A. J. Ptak, S. W. Johnston, S. Kurtz, D. J. Friedman, and W. K. Metzger. A comparison of MBE- and MOCVD-grown GaInNAs. *J. Cryst. Growth*, 251(1):392–398, 2003.

[139] A. Moto, M. Takahashi, and S. Takagishi. Hydrogen and carbon incorporation in GaInNAs. *J. Cryst. Growth*, 221(1):485–490, 2000.

[140] X. Li, S. E. Asher, S. Limpijumnong, B. M. Keyes, C. L. Perkins, T. M. Barnes, H. R. Moutinho, J. M. Luther, S. B. Zhang, S.-H. Wei, and J. C. Timothy. Impurity effects in ZnO and nitrogen-doped ZnO thin films fabricated by MOCVD. *J. Cryst. Growth*, 287(1):94–100, 2006.

[141] R. M. Lum, J. K. Klingert, D. W. Kisker, D. M. Tennant, M. D. Morris, D. L. Malm, J. Kovalchick, and L. A. Heimbrook. Investigation of carbon incorporation in GaAs using ^{13}C-enriched trimethylarsenic and $^{13}CH_4$. *J. Electron. Mater.*, 17(2):101–104, 1988.

[142] M. Hata, N. Fukuhara, Y. Zempo, M. Isemura, T. Yako, and T. Maeda. Residual impurities in epitaxial layers grown by MOVPE. *J. Cryst. Growth*, 93(1):543–549, 1988.

[143] P. Babelon, A. S. Dequiedt, H. Mostefa-Sba, S. Bourgeois, P. Sibillot, and M. Sacilotti. SEM and XPS studies of titanium dioxide thin films grown by MOCVD. *Thin Solid Films*, 322(1):63–67, 1998.

[144] M. R. Leys, M. E. Pistol, H. Titze, and L. Samuelson. On the growth of gallium phosphide layers on gallium phosphide substrates by MOVPE. *J. Electron. Mater.*, 18(1):25–31, 1989.

[145] P. M. Petroff. Transmission electron microscopy of interfaces in III–V compound semiconductors. *J. Vac. Sci. Technol.*, 14(4):973–978, 1977.

[146] M. S. Abrahams and C. J. Buiocchi. Cross-sectional specimens for transmission electron microscopy. *J. Appl. Phys.*, 45:3315, 1974.

[147] M. Moore. Synchrotron x-ray topography. *Radiat. Phys. Chem.*, 45(3):427–444, 1995.

[148] T. Tuomi, K. Naukkarinen, and P. Rabe. Use of synchrotron radiation in X-ray diffraction topography. *Phys. Stat. Sol. A*, 25(1):93–106, 1974.

[149] T. Tuomi. Synchrotron X-ray topography of electronic materials. *J. Synchrotron Radiat.*, 9(3):174–178, 2002.

Appendix 1: Experimental X-ray diffraction (XRD) and reflectivity (XRR) procedures

For the first XRD and XRR measurements, the sample was attached directly to the diffractometer with adhesive tape. Another attachment method was tried where the lightweight sample was attached to a heavyweight plastic plate with adhesive tape, and the plastic sample was attached to the diffractometer with adhesive tape. However, when using the heavyweight plastic plate, the measurements were unsatisfactory as the adhesive tape wasn't strong enough to hold the heavyweight plastic plate at a fixed location. Unfortunately, the samples were cut to smaller pieces when parts of the samples were sent for RBS/NRA analysis, so the measurements performed after RBS/NRA analysis were made with the heavyweight plastic plate. This had to be done, as the diffractometer sample cradle has a small hole in the middle of it, and only samples that are large enough can be attached directly to the diffractometer sample cradle with adhesive tape. Smaller samples need the plastic plate. When attaching the sample to the plastic plate, care was taken to avoid any residual forces which might result in curvature of the sample.

The angles of the detector were calibrated with the following procedure:

- A manual scan of intensity as a function of θ was made. At the maximum of the peak, θ was set to 0.0 deg. At this position, the radiation from the source goes directly into the detector. This calibration step needs to be done after

something in the optical path of the instrument has been modified, and it is good to check it in any case.

- The sample was attached to the sample holder of the diffractometer.
- The sample was moved along the Z axis (which happens to be one of the horizontal axes of the diffractometer) so that the sample obscured half of the beam going into the detector.
- The angle 2θ of the diffractometer was set to 0.2°. At this angle, total external reflection happens because the refractive index n of the material of the sample at X-ray frequencies is a bit smaller than 1. A manual scan of intensity as a function of ω was made. At the maximum of the peak, ω was set to 0.1° so that ω and θ are equal.

Additionally, for diffraction measurements the following additional calibration procedures were done:

- The ω and θ were aligned to the maximum of a diffraction peak.
- The sample was rotated 360° along an axis perpendicular to its surface. As a function of the angle Φ two peaks can be seen. The angle Φ was set to the midpoint of these peaks.
- The angle ω was aligned to the maximum of the diffraction peak again.
- A $2\theta - \omega$ scan was made which keeps the offset between θ and ω the same, and θ was aligned to the maximum of the diffraction peak.
- The angle ω was aligned to the maximum of the diffraction peak again.
- The sample was tilted along an axis parallel to the sample surface and in the same plane as the incident and diffracted wave. The angle Ψ was set to the maximum of the peak.
- The angle ω was aligned to the maximum of the diffraction peak again.

Appendix 2: A GNU Octave computer program to calculate composition of GaAsPN from E_+ and E_-

```
function result = bac(composition)
  global Eplus; global Eminus;
  y_As = composition(1); x_N = composition(2);
  EN = 2.18*(1-y_As) + 1.65*y_As;
  EMGamma = 2.776 - 1.469*y_As + 0.108*y_As**2;
  CMN = 3.05*(1-y_As) + 2.7*y_As;
  result = [
    0.5*((EMGamma+EN) + sqrt((EMGamma-EN)^2 + 4*x_N*CMN^2)) - Eplus
    0.5*((EMGamma+EN) - sqrt((EMGamma-EN)^2 + 4*x_N*CMN^2)) - Eminus
  ]';
end

global Eplus; global Eminus;
Eplus = input("E+ (eV): ");
Eminus = input("E- (eV): ");
composition = fsolve("bac", [0.3, 0.01]);
y_As = composition(1), x_N = composition(2)
```

Appendix 3: RBS and NRA measurement procedures

The RBS and NRA measurements were performed at Lawrence Berkeley National Laboratory by Kin Man Yu. In order to get accurate reference values for the compositions of the samples, the compositions were measured with channeling Rutherford backscattering spectroscopy (c-RBS) together with nuclear reaction analysis (NRA). To detect nitrogen, the ^{14}N(α,p)^{17}O reaction with a 3.72 MeV ^{4}He^{2+} beam was utilized. A passivated implanted planar silicon (PIPS) detector with an area of 150 mm^2 and a 3×12 mm slit was used to detect the emitted protons at 135° with respect to the incident beam. To absorb the backscattered alpha particles, a 25 μm thick mylar foil was placed in front of the detector. Simultaneously, RBS spectra were also measured at 165° with another PIPS detector. Both RBS and NRA measurements were carried out in random and <100> axial channeling directions. By comparing the random and channeling yields of the RBS and NRA measurements, it is possible to obtain the fraction of substitutional nitrogen atoms in the layers.

Appendix 4: PR measurement procedures

The measurement setup was configured in the following way before measurements:

- The power controller of the halogen lamp is set to a low value of 50 watts and the halogen lamp is situated so that it shines on the sample surface.
- The sample is rotated along the vertical axis so that the reflection of the halogen lamp from the sample goes to the lens in front of the monochromator. Additionally, a 409 nm filter is used in front of the monochromator to block scatter from the laser.
- The beam of the halogen lamp is chopped with a chopper and a lock-in amplifier is used to identify the signal from the halogen lamp at the frequency of the chopper. The signal of the chopper is connected to the lock-in amplifier as the reference frequency signal.
- The photodetector (a silicon PIN photodiode) which is connected to the lock-in-amplifier and is situated after the monochromator is moved to the position that gives the strongest signal to the lock-in-amplifier.
- The lens on front of the monochromator is also adjusted to the location which results in the strongest possible signal to the lock-in-amplifier.
- The InGaN laser diode operating at a low current of 30 mA is adjusted so that it shines on the sample surface.

Appendix 5: A GNU Octave function to calculate electron density of GaAsPN on GaP

```
% y and x are the As and N contents.
% zspace is the perpendicular lattice constant in meters.
% Example usage:
%   real_ed = 1.21659e+30;
%   zspace = 5.56120e-10;
%   y = 0.315; x = 0.00845709*(1-y); y,x,ed(zspace, y, x) - real_ed
%   y = 0.316; x = 0.00878483*(1-y); y,x,ed(zspace, y, x) - real_ed
% ...where the N contents corresponding to the As content have been
%    determined by fitting the location of the XRD peak using the XRD
%    software. zspace has been determined with XRD and real_ed by XRR.
% It can be observed that y=0.316 and x=0.006 gives the closest
% electron density.
function rho_e = ed(zspace, y, x)
  xyspace = 5.4505e-10;
  f_Ga = 29.71; f_As = 32.05;
  f_P = 15.30; f_N = 7.033;
  rho_e = (4*f_Ga+4*y*f_As+4*x*f_N+4*(1-x-y)*f_P)/(xyspace^2*zspace);
end
```